



Demonstration of soft stimulation treatments
of geothermal reservoirs

Deliverable 4.4:

Input data on business plan

Work package 4: Demonstration of combined hydraulic-thermal-chemical treatments in sandstones, carbonate rocks and granites.

Abstract

This report consists of three sections. The first section covers the experimental work that was carried out to analyse injectivity challenges at the DESTRESS demonstration sites and to provide detailed insight in their geological properties. Section two of this report presents an overview of the development of site-specific reservoir simulator development. Finally, section three contains a brief overview of the estimated costs of soft stimulation for the Trias Westland demonstration site in the Netherlands and the estimated costs of sampling and surveying to evaluate injection problems at the Mezőberény site in Hungary. This report therefore presents preparatory work for development of business plans for soft stimulation of poorly performing geothermal wells.



Lead Beneficiary	University of Glasgow
Type	<input checked="" type="checkbox"/> R - report, document etc. <input type="checkbox"/> OTHER - software, technical diagram etc. <input type="checkbox"/> DEM - demonstrator, pilot etc. <input type="checkbox"/> E - ethics <input type="checkbox"/> DEC - website, patent filing etc.
Status	<input type="checkbox"/> Draft <input checked="" type="checkbox"/> WP manager accepted <input type="checkbox"/> Project coordinator accepted
Dissemination level	<input checked="" type="checkbox"/> PU - Public <input type="checkbox"/> CO - Confidential: only for members of the consortium
Contributors	<input checked="" type="checkbox"/> 1-GFZ <input type="checkbox"/> 5-GES <input checked="" type="checkbox"/> 9-GTL <input type="checkbox"/> 13-SNU <input type="checkbox"/> 2-ENB <input checked="" type="checkbox"/> 6-TNO <input checked="" type="checkbox"/> 10-UoS <input type="checkbox"/> 14-KIC <input type="checkbox"/> 3-ESG <input checked="" type="checkbox"/> 7-ETH <input checked="" type="checkbox"/> 11-TUD <input type="checkbox"/> 15-ECW <input checked="" type="checkbox"/> 4-UoG <input type="checkbox"/> 8-GTN <input type="checkbox"/> 12-NEX <input checked="" type="checkbox"/> 16-WES
Creation date	20.02.2020
Last change	27.02.2020
Version	6.2
Due date	29.02.2020
Submission date	24.03.2020

Authors

Cees Willems (UoG), Rob Westaway (UoG), Neil Burnside (UoG), Sean Watson (UoG), Aaron Williams (UoG), David Walls (UoG), Jan ter Heege (TNO), Xiang-Zhao Kong (ETH), Jin Ma (ETH), Diego Denzler (ETH), Martin O. Saar (ETH), Nima Gholizadeh Doonechaly (TUD), Guido Blöcher (GFZ), and Antoine Jacquey (GFZ)

Context and objectives

Detailed reservoir performance analyses, reservoir property quantification and reservoir simulation tools are crucial for planning and design of soft stimulation techniques. This report presents an overview of the experimental work on injection problems and geological conditions at the DESTRESS demonstration sites. It also covers the development of site specific, tailor-made reservoir simulators. Both the simulators and the experimental work provide the basis for soft stimulation design, decision making and business models.

This work is part of DESTRESS Work Package 4 'Demonstration of combined hydraulic-thermal-chemical treatments in sandstones, carbonate rocks and granites'. It is concerned with investigation of the effectiveness of stimulation techniques that aim to safely increase efficiency of poorly performing geothermal wells. Hydraulic, thermal, and chemical stimulation techniques are considered, depending on the specific challenges at the different demonstration sites. Reservoir simulators have been developed for the DESTRESS demonstration sites at Mezőberény (Hungary), Soultz-sous-Forêts (France), Klaipeda (Lithuania) and Westland (the Netherlands). This report covers in detail the experimental work related to the Mezobereny and Klaipeda sites. Experimental work related to the Soultz-sous-Forêts site is reported separately as part of Deliverable 4.3. Experimental work related to the Westland site is reported separately as Deliverable 4.2, but a brief summary is included here.

This experimental work focussed on rock characterisation. It has included identification of mineralogy, thermal properties, permeability and porosity of the aquifers. It has also included thin section analyses, scanning electron microscopy, x-ray computed tomography, thermal property measurements and gas pycnometry. Reactive flow-through experiments have also been conducted for the Mezőberény site to assess the potential of chemical stimulation. This work not only provides input for other DESTRESS work packages, it also significantly extends the available aquifer property data for Pannonian Sandstones, the Dutch Triassic Buntsandstein Subgroup, and Devonian strata in Lithuania and Latvia, which will aid future researchers and project developers in quantifying geothermal potential in those regions. Section 1 of this report presents an overview of all the experimental work.

This report also presents an overview of the development and validation of tailor-made numerical reservoir simulators. This aspect is discussed and explained in Section 2. These simulators are capable of incorporating thermal, chemical and hydraulic stimulation, depending on the specific injection challenges of the different demonstration sites. They allow cost-benefit analyses of soft stimulation and optimization of stimulation design. Finally, estimated breakdowns of costs are presented in Section 3 for the planned soft stimulation at the Westland site and for the costs for logging and evaluation of injectivity problems for the Mezőberény site. These data support the financial analyses in Work Package 2 of DESTRESS.

Contents

1.	Experimental rock characterisation	5
1.1	Mezőberény, Hungary	5
1.1.1	Introduction	5
1.1.2	Core and log data Újfalú Formation	5
1.1.3	Rock characterisation methods	8
1.1.3.1	X-CT Imaging of Mezőberény Samples	8
1.1.3.2	Petrographical analysis and SEM	10
1.1.3.3	Porosity with pycnometry and pore size distribution with porosimetry	10
1.1.3.4	Reactive flow through experiment	11
1.1.4	Results of experimental rock characterisation for Mezőberény	11
1.1.4.1	Petrographical analysis and SEM samples H1 to H4	11
1.1.4.2	Pore size distribution and porosity	17
1.1.4.3	Permeability and reactive flow-through results	17
1.1.4.4	X-CT results	20
1.1.4.5	Numerical flow through experiments	22
1.2	Westland, the Netherlands	26
1.3	Klaipėda, Lithuania	27
1.3.1	Geological overview	27
1.3.2	Fieldwork sample acquisition	27
1.3.3	X-CT Methodology	28
1.3.4	X-CT Results	30
1.3.5	Discussion and Conclusion on X-CT analysis	30
1.3.6	Mineralogy, porosity and flow through experiments	31
1.3.7	Conclusion flow through experiments	41
2.	Reservoir simulator development	42
2.1	Thermal-hydraulic simulator for Klaipėda	42
2.2	Thermal-hydraulic simulator for Mezőberény	44
2.3	Thermal-hydraulic-mechanical simulator Trias Westland	45
2.4	Thermal-hydraulic simulator for Soultz-sous-Forêts	46
3.	Input data for the business plan - costs for stimulation	51
4.	Conclusions	53

1. Experimental rock characterisation

1.1 Mezőberény, Hungary

Cees Willems, Sean Watson, Aaron Williams, David Walls, Neil Burnside, Rob Westaway, Jin Ma, Xiang-Zhao Kong, Diego Denzler, and Martin O. Saar

1.1.1 Introduction

Hundreds of geothermal wells have been drilled in Hungary in past decades for direct-use applications. Roughly half of these are used for spas and the other half for district-, agriculture- or industrial heating (e.g. Nador et al., 2016). Deltaic and turbiditic sandstones deposited during the Pannonian stage of the Late Miocene form one of the main geothermal targets in the Pannonian Basin (e.g., Szanyi and Kovács, 2010; Toth, 2015; Nador et al., 2016). These rocks were deposited during a time of dramatic environmental change, resulting in rapidly-changing sedimentary environments: the ancestral southward drainage of the Pannonian Basin to the Aegean Sea became disrupted, creating an endoreic lacustrine environment, before the modern drainage to the Black Sea via the River Danube became established (Csato et al., 2007; Olariu et al., 2018; Sztanó et al., 2013). Despite the long experience with geothermal heat production from these aquifers, reinjection issues are common and fewer than 10% of all Hungarian geothermal wells are reinjection wells; most projects discharge at the Earth's surface (Szanyi and Kovács, 2010; Toth, 2015). Without reinjection, aquifer pressure has reduced significantly in recent decades at most geothermal sites, limiting efficient and sustainable exploitation of these geothermal resources (Szanyi and Kovács, 2010). Chemical factors, such as scaling and clay mobilization, have previously been discussed as causes of the injection problems (Balint et al., 2010; Nador et al., 2016).

1.1.2 Core and log data Újfalu Formation

A subsurface dataset from the Békés Basin in southeast Hungary has formed the basis for the experimental rock characterisation. This dataset comprises of two Gamma-Ray (GR) logs for the Mezőberény doublet, five legacy GR logs for nearby petroleum wells, core fragments from the Gyoma-1 and Kond-1 wells, and six 2D seismic lines (Figure 1). Core fragments were also obtained from the MOL Group core repository in Szolnok, Hungary. Four samples from the Újfalu Formation were acquired and brought to the UK for experimental work. One sample was a homogeneous medium-grained sandstone, the other three comprised fine-grained sandstone and siltstone. Well logs were obtained from the archive managed by the Hungarian Geological Survey in Budapest.

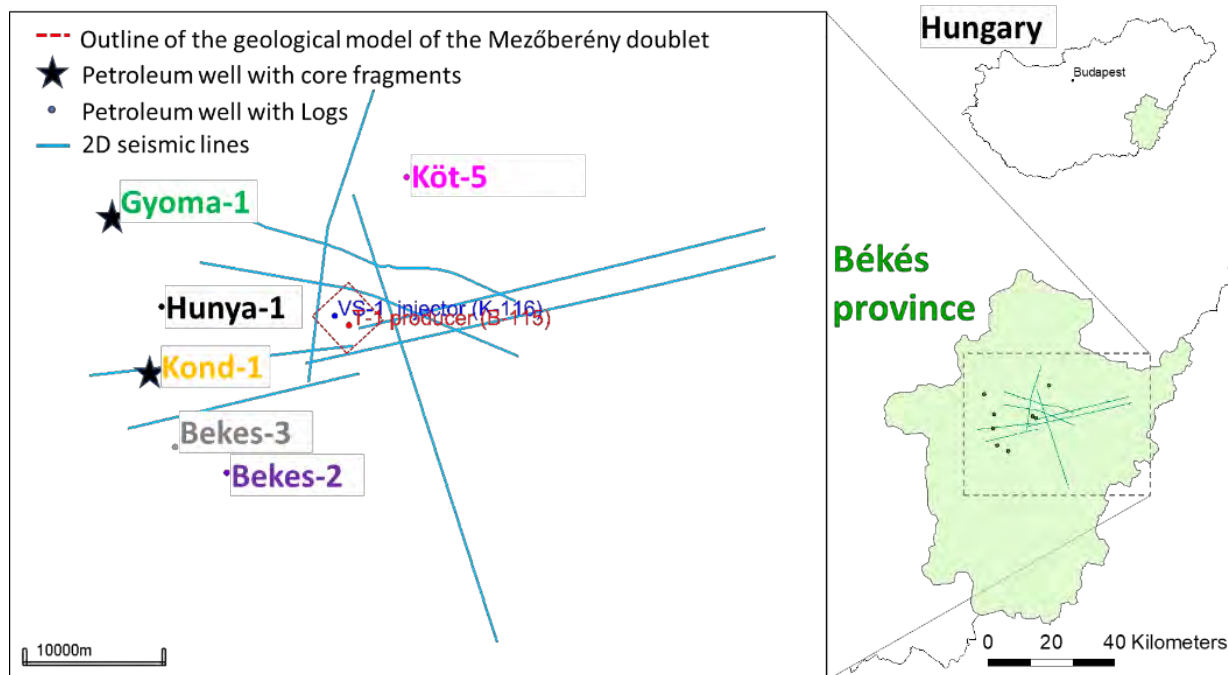


Figure 1: Location of the Békés Basin in Hungary, and the outline of our study area with the location of the seismic lines, the Mezőberény doublet and nearby petroleum wells. Core fragments from the Újfalu Formation were available from the Gyoma-1 and Kond-1 wells.

Rock characterisation was based on core fragments from the Gyoma-1 and Kond-1 wells. These are petroleum wells, located ~10 km from the Mezőberény geothermal doublet (Figure 1). To confirm that these samples were deposited as lateral equivalents of the geothermal aquifer, a regional well log correlation was made, based on recognition of net-to-gross trends in the GR logs. The INPEFA method was applied to recognise GR trends. INPEFA identifies discontinuities in GR log data, which can be interpreted as sequence stratigraphic changes (ENRES, 2011). We assume that the regional GR log trends that are consistently recognised can be related to lake-level fluctuations, thus influencing the distal lacustrine facies of the Pannonian Sandstones. Changes in sedimentation rate and grain size are reflected by turning points in INPEFA logs. At these turning points, the INPEFA curves change between leftward and rightward trends going upward across the logs. INPEFA curves and GR logs in Figure 2 show high readings at depths of ~2000 m. This is related to more distal, fine grained lacustrine sedimentation. The turning point at which the sandstone content of shallower intervals starts to increase is highlighted by the red INPEFA curve in Figure 2. This point marks the start of the well log correlation. Sandstone content increases above this turning point, which could be interpreted as a consequence of relative lake level fall and more proximal, sandstone-rich sedimentation. A second regional turning point is recognised around 1750 m (green line in Figure 2). Above this, INPEFA curves do not show consistent trends, which we relate to more heterogeneous sedimentation in an environment increasingly resembling a coastal plain. Recognition of the turning points as correlation markers suggests that core samples H1-5 are indeed lateral equivalents of the geothermal aquifer in Mezőberény.

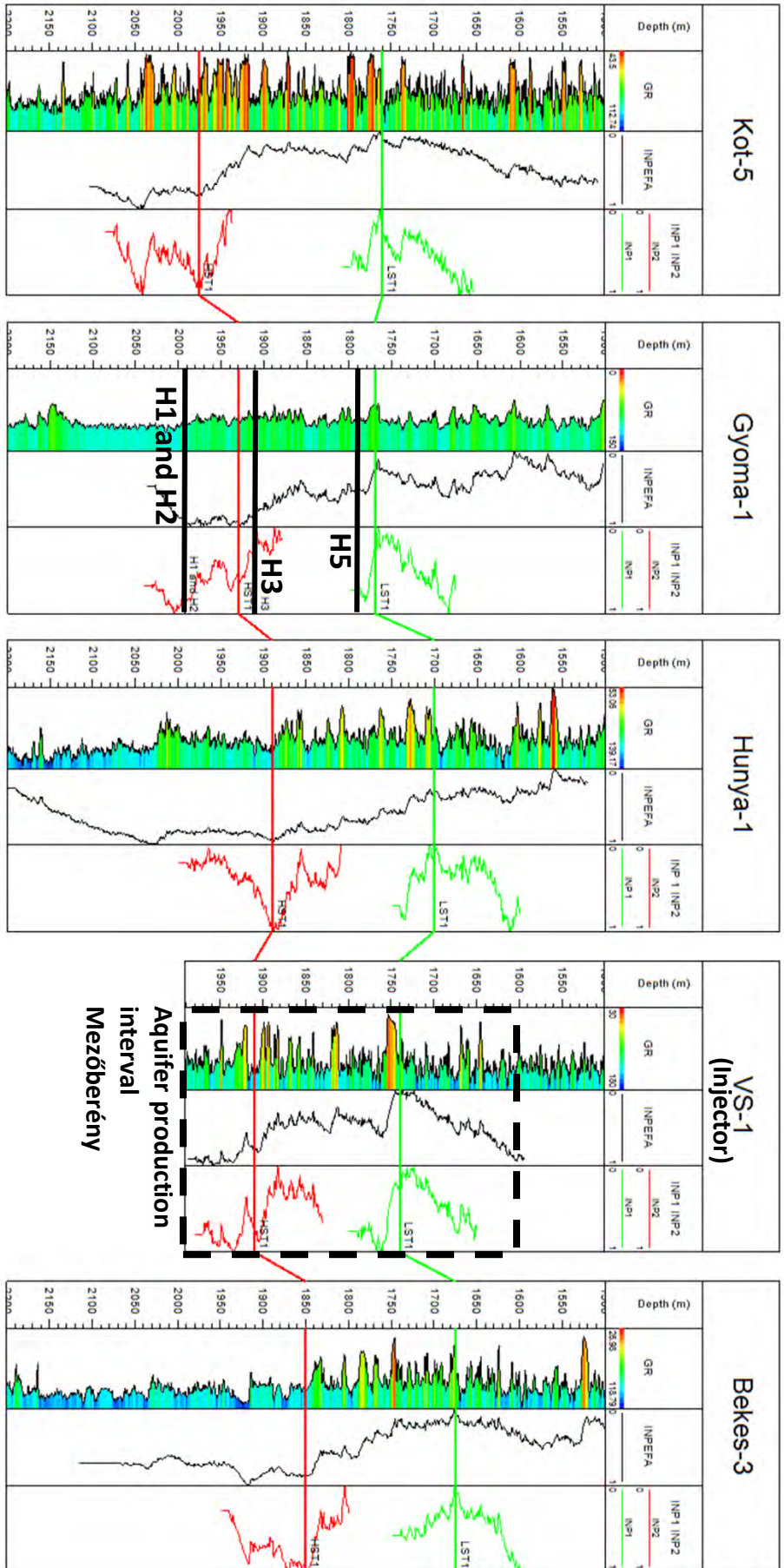


Figure 2: Regional GR well log correlation, well locations in Figure 1. Only one well of the Mezőberény doublet is displayed (VS-1). Blue colours in the GR logs indicate fine grained sediments, red colors indicate coarser grained sandstones. No GR log was available for well Kond-1 and therefore this well is not displayed in the panel. Depth of the core fragments from which samples were derived for the experimental rock characterisation are indicated by thick black lines in well Gyoma-1.

1.1.3 Rock characterisation methods

Table 1 presents a summary of the experimental methods that were applied to core fragments H1 to H5 and the properties derived from the individual analyses. The following sub-sections present explanations of experimental methods.

Table 1: Overview of experimental analyses applied to core samples H1 to H5.

sample	H1	H2	H3	H4	H5	
Well	Gyoma-1	Gyoma-1	Gyoma-1	Kond-1	Gyoma-1	
Depth [m]	1990-1995	1990-1995	1910-1913	1500	1796-1801	
Facies	Fine-grained sst.	Fine-grained sst.	Medium grained sst.	Fine-grained sst.	Shale	
Analyses						Property
X-CT	Y	Y	Y	Y		Porosity
Thin section	Y	Y	Y	Y	Y	Minerology
Scanning Electron Microscope (SEM)	Y		Y	Y	Y	Minerology
Mercury Intrusion Porosimetry (MIP)	Y		Y	Y		Porosity, density
Differential Scanning Calorimetry (DSC)	Y		Y	Y		Heat capacity
Laser Flash Analyser (LTA)	Y		Y	Y		Thermal conductivity
Reactive flow-through				Y		Permeability
Numerical flow-through simulation			Y			Permeability
Gas Pycnometry (GP)			Y	Y		Porosity

1.1.3.1 X-CT Imaging of Mezőberény Samples

X-ray computed tomography (X-CT) is a non-destructive and non-invasive method which uses contrasts of x-ray attenuation (a function of density and atomic number) to reconstruct the 3D distribution of areas of different densities within a large variety of materials. The 3D reconstruction is based on a series of contiguous 2D radiographs taken with different view angles, by rotating a sample around a single axis in small steps. X-CT has been increasingly used in Earth Science over the past two decades (Ketcham and Carlson, 2001; Cnudde and Boone, 2013). Amongst many other examples, X-CT analysis has been successfully utilised to unravel the shape, orientation and 3D distribution of minerals,

porosity and cracks in sedimentary rocks (e.g., Noiriél, 2015). The objective of this analysis was to estimate the porosity and assess the possible presence of cementation or clay fines blocking the pore space within the borehole core samples.

The X-CT scans were performed using a Nikon XTH 320/225 system, equipped with a 225 kV reflection gun and a 2000 × 2000 pixel flat panel photodetector (cell size 0.2 × 0.2 mm). The scanning conditions are summarised in Table 2. To begin with, an accelerating voltage of 150 kV was used for each sample with 40 µA current, apart from sample Gyoma 1990 B where a 53 µA current was used. For the first round of scans, the x-ray source-to-sample distance was set to achieve an approximate minimal voxel size of 7 µm, as shown in Table 2. A final scan was conducted to scan a small sub-sample of Gyoma 1910 to analyse this sample at a higher resolution. For this scan, an accelerating voltage of 140 kV and 19 µA current was used. No filters were used for these scans. The exposure time for each projection was 1.41 s, repeated for 3141 projections.

Table 2: X-CT scan conditions.

Name	Voxel size (µm)	Scan Size (Voxels)	Voltage (kV)	Current (µA)
H1	7.48	1684 × 1436 × 1592	150	40
H2	8.79	1494 × 1556 × 1779	150	53
H3	7.15	1590 × 1751 × 1866	150	40
H4	6.52	1609 × 1370 × 1936	150	40
H3 High Res.	2.79	2000 × 2000 × 1399	140	19

To ensure accurate quantitative results it is necessary to have high quality images that avoid sources of error, such as artefacts due to the image reconstruction process. 3D volumes were reconstructed from projections using the CT Pro 3D software (© 2004-2016 Nikon Metrology), with an automatic reconstruction tool to find the centre of rotation of a scan and to apply a beam hardening correction (Brooks and Dichiro, 1976). Ring artefacts, which are common in micro X-CT, affected the segmentation process, but this was mitigated by removing the slices affected. All volumes were reconstructed to 16 bits (65536 greyscale values).

The 3D volumes were processed using Dragonfly software (v. 4.1.0.647, © Object Research Systems (ORS) Inc.) to reconstruct the surfaces of the sandstone samples. To reduce the effects of ring artefacts and beam hardening at the edges of each sample, a sub-volume within the sample was created using the “crop” tool. This allowed mitigation of the aforementioned affects as well as limiting the opportunity to segment external air, focusing on the internal pore space.

The phases (mineral and pore) were separated manually using simple greyscale thresholding, by segmentation of the volumes corresponding to the relative density range of each individual phase. Segmentation is considered optimal when the selected range of grey values selects all the voxels belonging to the pore phase while avoiding voxels that belong to the mineral phase. Such optimal separation is achieved due to the strong contrast between the phases. The software determines the volumes of the mineral phase and pore phases by “counting” the voxels in the respective voxel clusters. The choice of grey scale value used to segment the pores and the mineral phases influences the resulting value of porosity determined within the sample volume. To achieve the optimal value, a sensitivity analysis was conducted to determine the porosity using numerous grey scale values to represent the segmented pore space.

1.1.3.2 Petrographic analysis and SEM

The thin sections of the samples H1 to H4 were analysed for their mineral and textural properties. The composition of the grains and cement within these samples was determined using plane- and cross-polarised light. Grain size has been estimated by counting the number of grains present in the field of view. Grain shape has been given as the approximate average roundness of the grains from very angular to well rounded. The sorting of each sample has been determined from the consistency of grain size, where well sorted means little variation and poorly sorted means a significant variation.

Using Scanning Electron Microscopy (SEM), the type, origin, and distribution of clays were identified within samples H1, H3 and H4. The primary method for identifying which clays were present was energy dispersive x-ray analysis (EDXA), which was backed up, where possible, by optically recognising morphological features of the clays. In preparation for the SEM analysis, the thin sections were given a carbon coating. This coating was detected by the EDXA, which has the potential to cause problems with the identification of some minerals. However, as carbon is not a constituent of any clay type, it did not present an issue for the present analysis. The small pieces of sample, which were analysed alongside the thin sections, were prepared by breaking them open and immediately coating them with gold to preserve the material. As for the carbon coating, the gold was detected in the EDXA, but again gold is not a constituent of clays and so it did not present an issue with identification.

1.1.3.3 Porosity by pycnometry and pore size distribution by porosimetry

Two of the sandstone samples, H4 and H3, were used for this study. Sample H4 is of consolidated sandstone from a depth of 1500 m in well Kond-1. It was cored to produce a cylindrical specimen (Figure 3) of diameter 25.07 mm and length 20.57 mm, for porosity measurement and flow-through (acid stimulation) experiment. Sample H3 is unconsolidated sandstone from a depth of 1910-1913 m in well Gyoma-1. It was cut to produce a cuboidal specimen (Figure 3) with dimensions of 10.30 × 11.58 × 9.95 mm for porosity measurement.

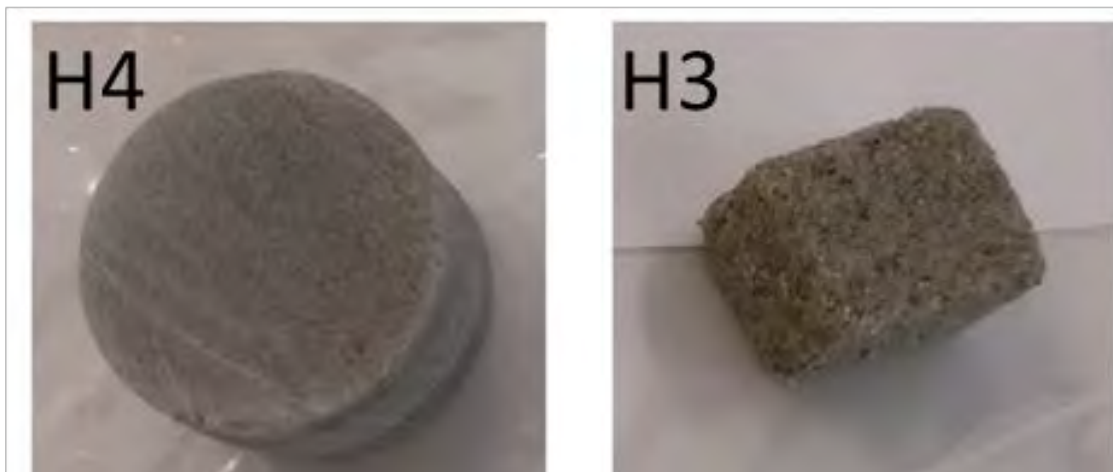


Figure 3: Samples H4 and H3.

The solid volumes of the two samples have been determined using a gas pycnometer (Micromeritics AccuPyc II 1340), using helium at a temperature of 25.2 - 25.8 °C, in the Rock Deformation Laboratory at ETH Zurich. Pore size distribution (PSD) of these samples has been obtained using mercury intrusion porosimetry. The PSD measurement was carried out at 22.6 °C and a maximum pressure of 400 MPa using the Porotec Pascal 140 and 440 apparatus in the IGT Claylab at ETH Zurich.

1.1.3.4 Reactive flow through experiment

Permeabilities of samples H4 and H3 at zero effective stress ($P_{\text{confining}} - P_{\text{pore}} = 0$) were estimated from their pore size distributions using the following equation (Marshall, 1958):

$$k = \phi^2 n^{-2} [r_1^2 + 3r_2^2 + 5r_3^2 + \dots + (2n - 1)r_n^2] / 8$$

where k is the permeability in cm^2 , ϕ is porosity, n is the number of equal pore volume fractions and r is the mean radius in cm of each pore volume fraction. Taking $n=10$, the permeabilities are estimated to be $4.93 \times 10^{-18} \text{ m}^2$ (H4) and $4.92 \times 10^{-13} \text{ m}^2$ (H3).

Flow-through experiments were performed on the cylindrical specimen from sample H4 to investigate its permeability under reservoir stress and formation fluid salinity. The equivalent of the formation fluid was around 80 mEq/l, according to the fluid chemistry report (Vízkezelő Vízkezelés, 2012). Thus, a solution of 80 mmol/l (4.68 g/l) NaCl was prepared for the permeability measurement, to minimize the potential effect of clay swelling. After the flow-through system (including the sandstone specimen) was vacuumed, it was saturated with this NaCl solution. Considering the reservoir depth (1500 m) of Sample H4, a constant outlet/back pressure was set to 150 bar and a constant confining pressure to 340 bar. However, the working temperature was set as the room temperature (rather than the ambient temperature at the sample depth) to prevent corrosion of the tubing.

1.1.4 Experimental rock characterisation for Mezőberény

1.1.4.1 Petrographical and SEM analysis for samples H1 to H4

Samples H1 and H2 are arkosic arenite siltstones. H1 shows a clear upward coarsening structure. Grains range in size from medium silt ($\sim 20 \mu\text{m}$) to coarse silt ($\sim 40 \mu\text{m}$) in the upper part of the sample (Figure 4A). The grains are dominantly angular to sub-angular though some sub-rounded grains are present (Figure 4C). Especially in sample H2, significant calcite cementation was recognised (Figure 4D). Using optical interpretation, the mineralogy of this sample is estimated to consist of 60% quartz, 10% potassic feldspar, 10% mica, and 20% clay. The fine grain size and mineral content suggest that the sediments were deposited in a low energy environment. The grains have linear and concave contacts, suggesting that the rock has experienced moderate compaction. Significant amounts of chlorite, illite, and kaolinite significantly reduce porosity (Figure 4E and F).

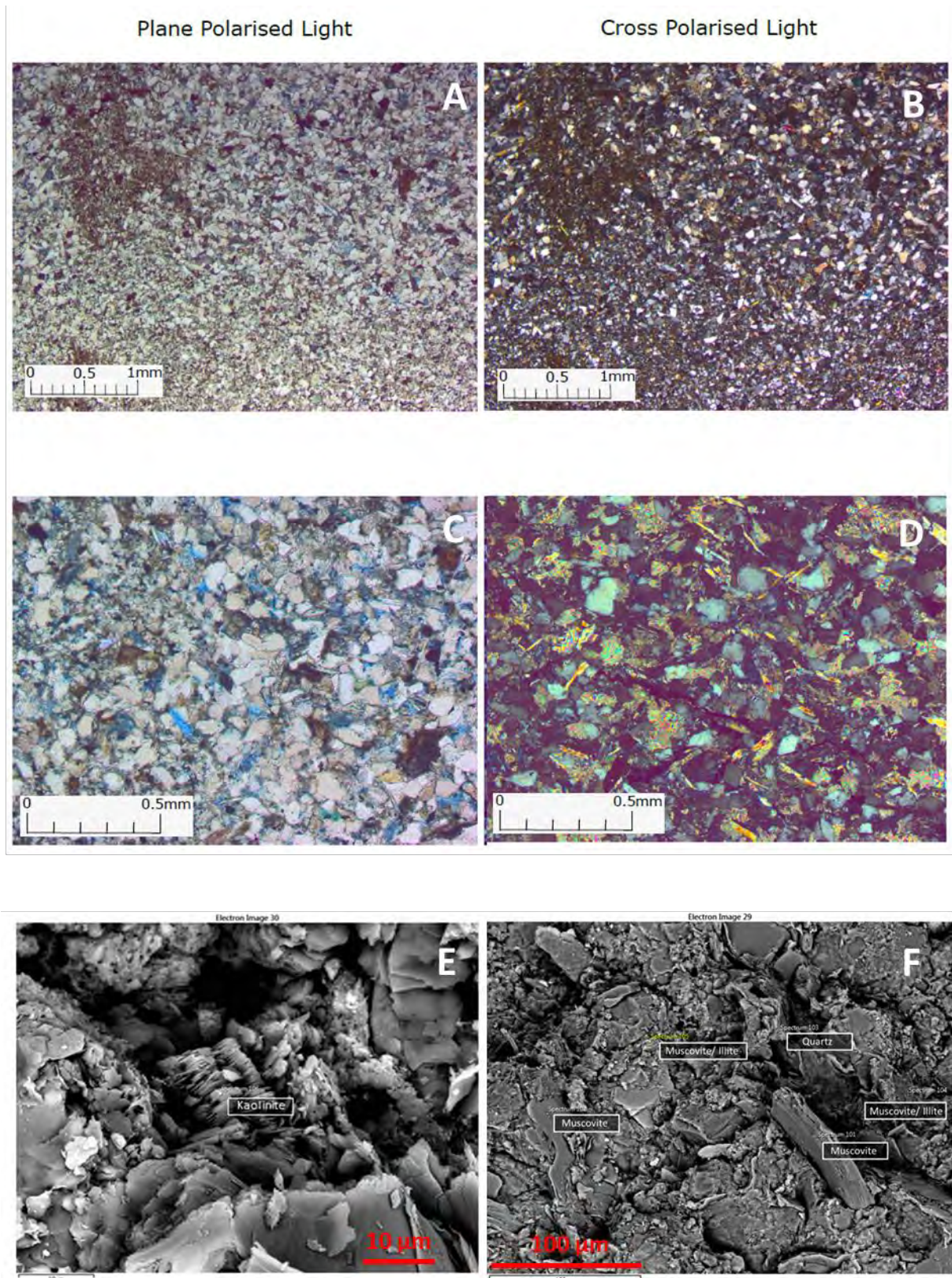


Figure 4: Photomicrographs of sample H1 (A-C) and sample H2 (D) and SEM image of sample H1 (E and F).

Sample H3 is a feldspathic quartz arenite sandstone with fine ($\sim 125 \mu\text{m}$), angular to sub-rounded, well sorted grains (Figure 5A to D). This material comprises $\sim 60\%$ quartz and 40% potassic feldspar grains with little to no cementing. Contacts between grains are dominantly linear and concave, suggesting moderate compaction. The coarser grain size of this sandstone compared with the other samples, along with a lack of internal structure, suggest deposition in a moderate energy environment. Sample H3 displayed the best aquifer properties of all the samples, having little to no cement and clay minerals. The clay present was predominantly kaolinite; small amounts of chlorite, illite, and montmorillonite were also identified (Figure 6). Montmorillonite was observed alongside illite (Figure 6A). A small amount of authigenic quartz was also observed (Figure 6B), which may be a side-product of the transformation of montmorillonite to smectite. This transformation produces silica in solution, which could be deposited as authigenic quartz and reduce porosity and permeability in the aquifer. However, a larger threat to permeability is the fairly common presence of kaolinite. A small amount of material that might possibly be authigenic quartz was also observed (Figure 6C and D). This mineral is easily mobilised and could therefore clog pore space and reduce the permeability, depending on flow speeds and salinity of the injected water.

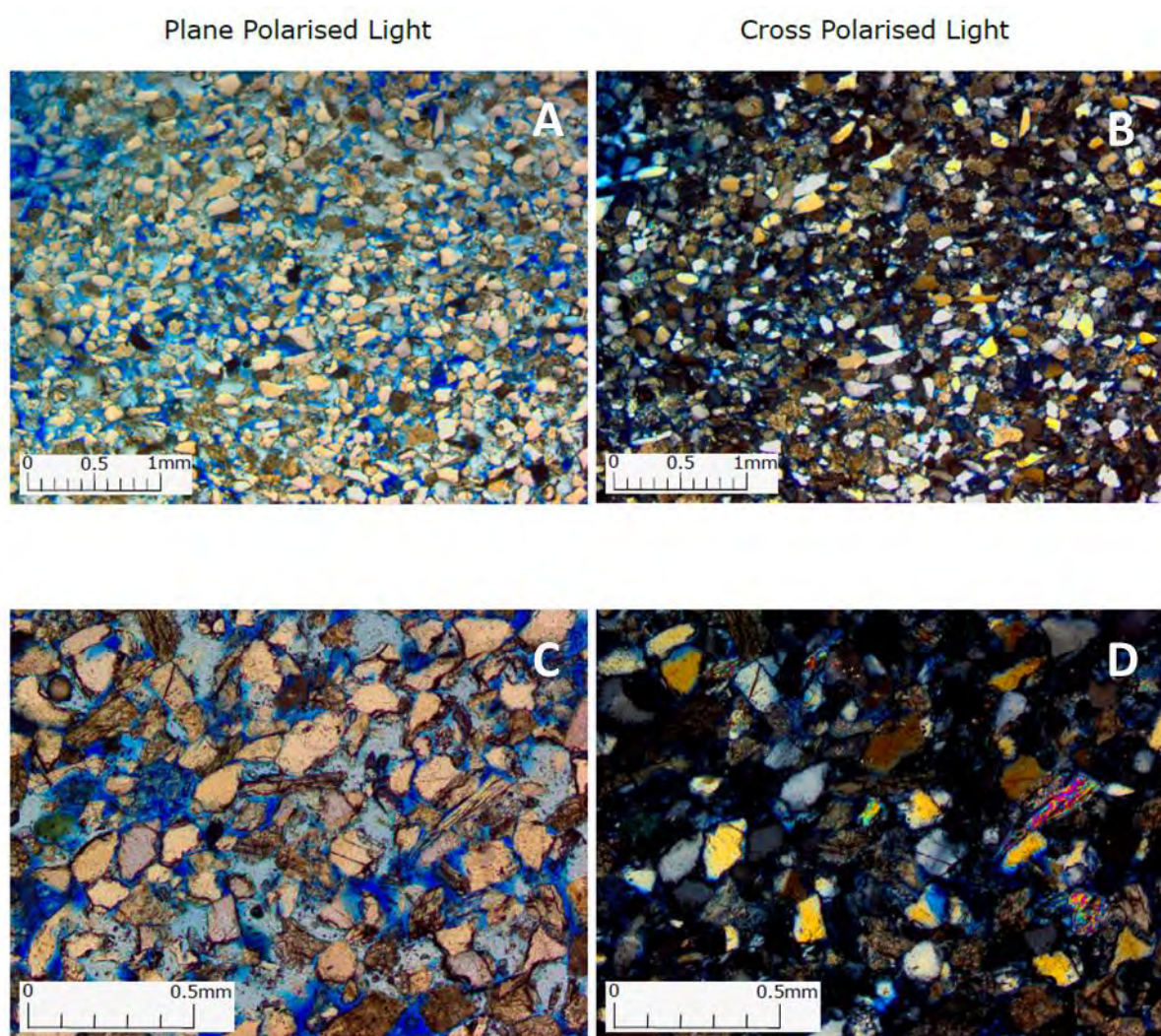


Figure 5: Photomicrographs of sample H3.

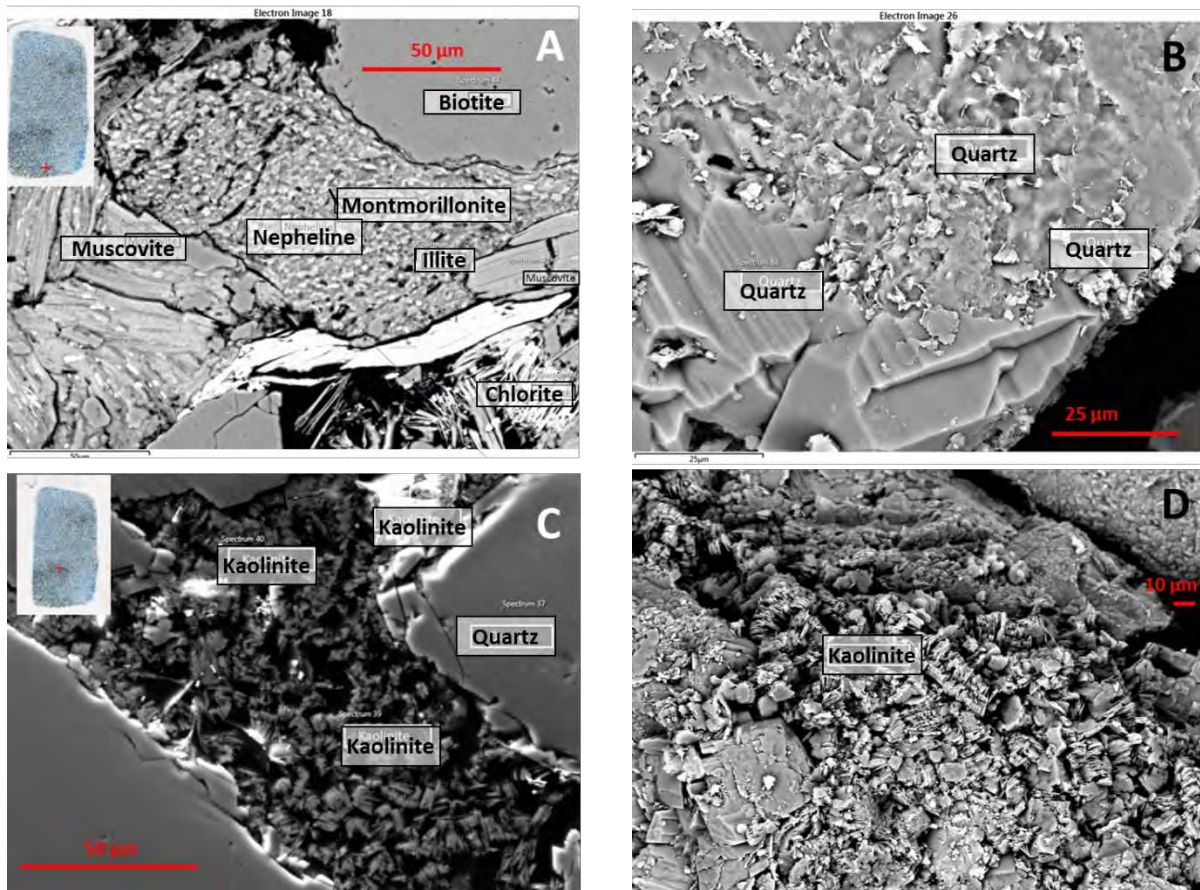
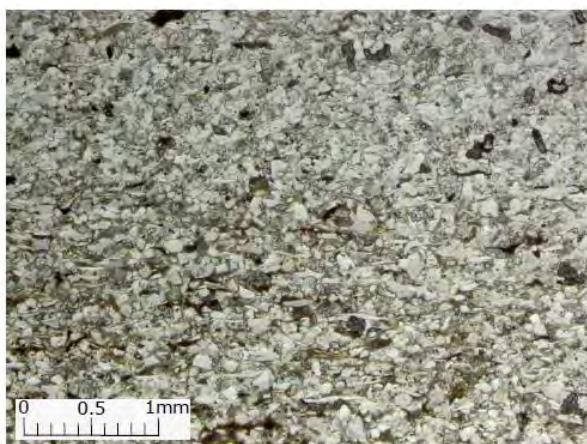


Figure 6: SEM and EDXA images from the thin section of sample H3.

Sample H4 is a heavily calcite cemented siltstone with little porosity. Silt grains are $\sim 50 \mu\text{m}$ and many clay minerals are recognised. Overall, this material comprises 45% quartz, 5% mica, 30% calcite cement, and 20% clay. The grains are angular to sub-rounded, suggesting a short transport distance between source and deposition. Fine laminations within this sample, along with the fine grain size, suggest sedimentation in a low energy environment. Linear contact points between the quartz grains and bending within the micas suggest that the sediment has been moderately compacted. The distribution of calcite cement suggests that it was deposited as a calcite-rich mud; the calcite later re-crystallised into calcite cement following burial.

Plane Polarised Light



Cross Polarised Light

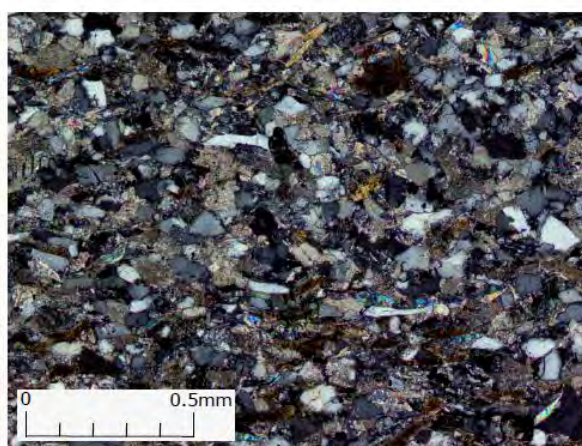
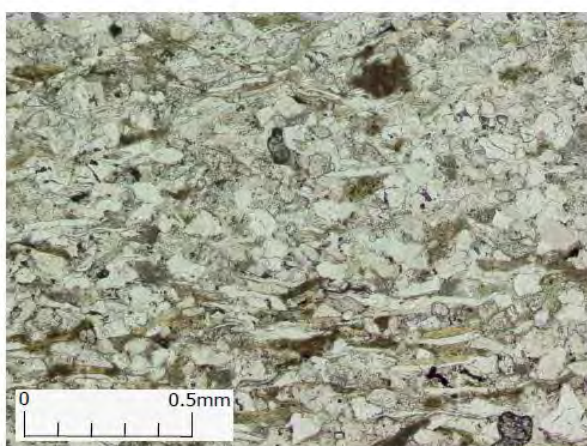
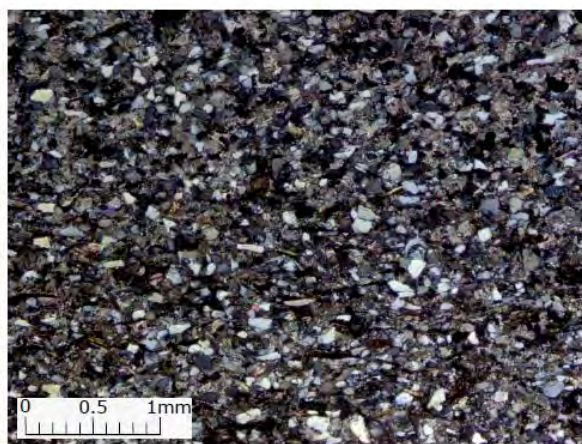


Figure 7: Photomicrographs of sample H4.

Sample H5 predominantly comprises clay with minor amounts of quartz and mica silt. The grains present are mostly $<20\ \mu\text{m}$ although some are as large as $50\ \mu\text{m}$ (Figure 8A to D). The predominance of clay in this sample suggests that it was deposited in a very low energy environment, either offshore or in the floodplain of the palaeo-delta. With the SEM, an abundance of muscovite is recognised. Other minerals recognised include albite, biotite, phlogopite and illite. Illite is mainly recognised near crumbling edges of decomposing muscovite flakes, suggesting that it has been formed by decomposing muscovite.

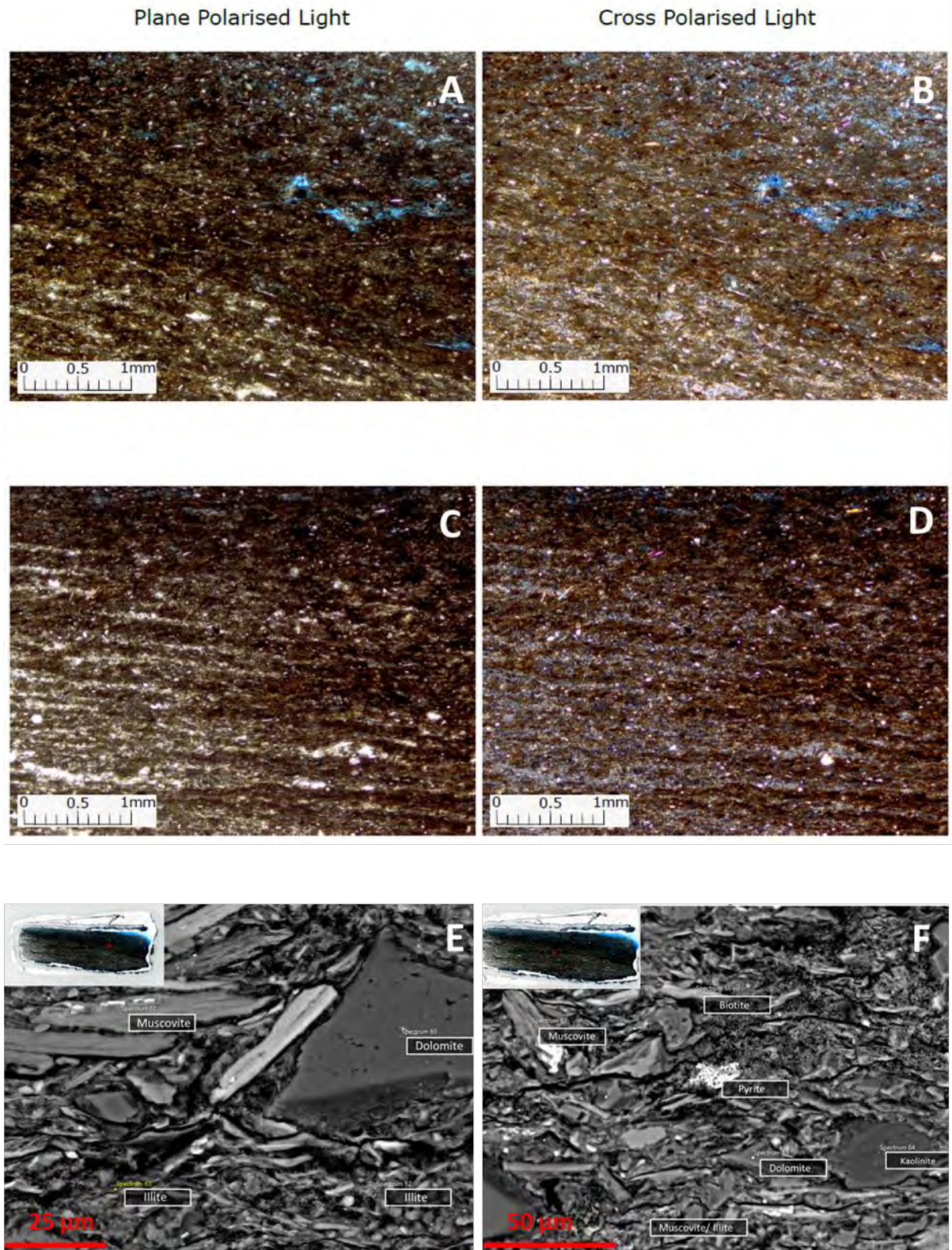


Figure 8: Photomicrographs (A to D) and SEM images (E and F) of sample H5.

1.1.4.2 Pore size distribution and porosity

Pore size distribution and porosity were analysed for samples H4 and H3 (Fig. 9). The blue curves in Figure 9 show the pore size distributions of these samples, with a detectable diameter range of 3.7 nm to 0.114 mm. The dominant pore sizes are 200-400 nm for sample H4 and 20-40 μm for sample H3. The orange curves depict the variations of cumulative pore volume with pore size. In general, the maximum cumulative pore volume is a good indicator of porosity: this is much lower for H4 than for H3. This observation is consistent with the porosity measurements, 9.39% for H4 and 38.76% for H3.

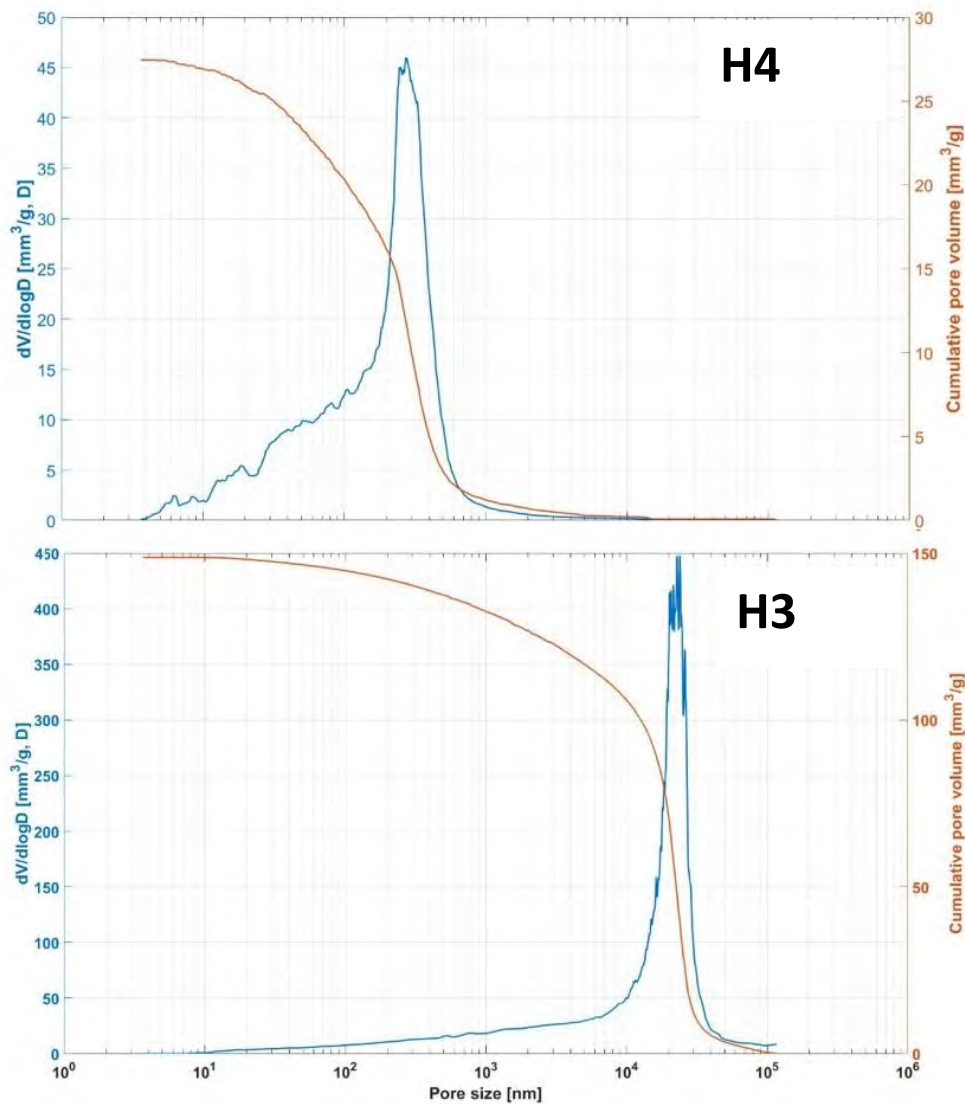


Figure 9: Pore size distributions from mercury porosimetry for samples H4 and H3.

1.1.4.3 Permeability and reactive flow-through results

The differential pressure measurements, between the inlet and the outlet, for the reactive flow-through experiment on sample H4, is shown in Figure 10. In the first two hours of the measurement, different flow rates were tested. Later an optimum flow rate of 0.003 ml/min was found and the measurement run for ~ 22 hours. A steady state was reached at a differential pressure of 11.1 bar, which yields a permeability at reservoir stress of $1.72 \times 10^{-18} \text{ m}^2$ using Darcy's law, assuming a viscosity of 919.7 $\mu\text{Pa s}$ for the NaCl solution (Bando et al, 2004).

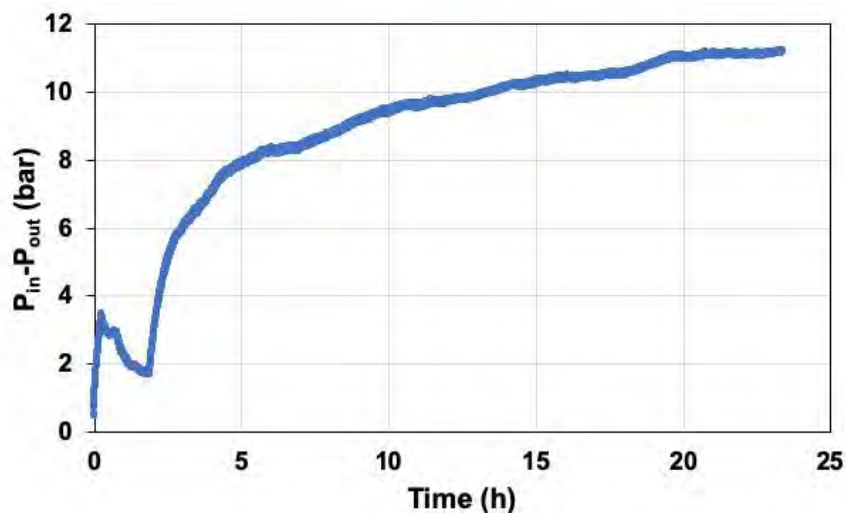


Figure 10: Evolution of the differential pressure between the inlet and the outlet during permeability measurement for sample H4.

1.1.1.4.4 Permeability and reactive flow-through results

The acid solution used in the acid stimulation experiment was the same NaCl solution (80 mmol/l NaCl) but with 10 mmol/l HCl added. This acid solution was injected at a rate of 0.01 ml/min into sample H4 at the same outlet and confinement pressures and temperature as the permeability test (Figure 10). This experiment was run for >250 hours. However, after ~74 hours, a small leak was identified at the inlet. Results are therefore only presented for the first 74 hours (Figure 11). Overall, the permeability experienced a slight overall decrease during this experiment, along with fluctuations.

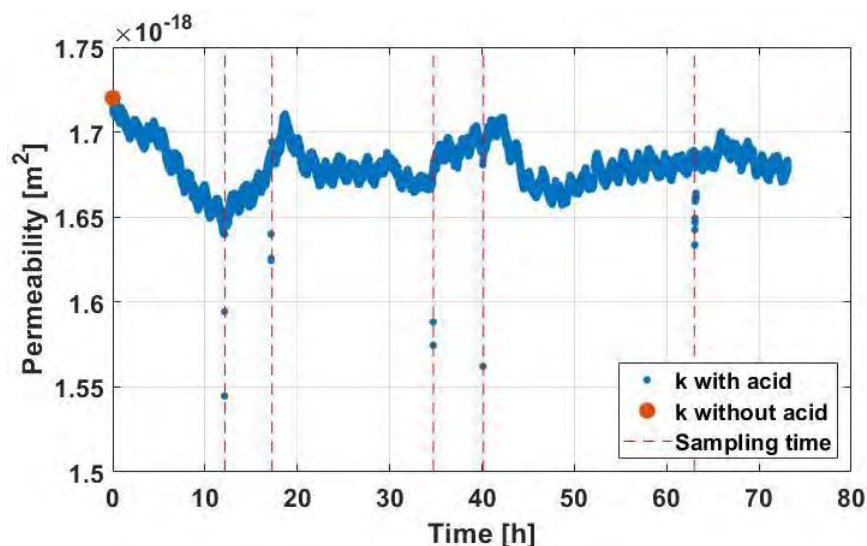


Figure 11: Permeability evolution for sample H4 during the acid injection. The initial permeability is plotted as an orange dot at time zero. The scattered blue dots below the blue curve, at times indicated by dashed lines, are perturbed measurements due to sampling of the outlet fluid for chemical analysis. The observed overall decrease in permeability was unexpected; the aim of this experiment was to simulate the effect of acid stimulation, with the objective of increasing permeability.

A total of 12 effluent samples were collected at the outlet during the 250-hour duration of the experiment. The effluent samples were analysed by ion chromatography, at the times indicated in Fig.

11, to infer the dissolution process. The measured concentrations of the major cations are shown in Table 3. Calcium (Ca) was found to be the most dominant cation (Figure 12). This is consistent with the XRD measurement on sample H4, indicating that calcite is the major carbonate in this sandstone sample. Sodium (Na) remains at its initial concentration of 80 mmol/l. Potassium (K) exhibits highly fluctuating concentrations: when pH was measured by a pH meter, the potassium concentration was high. We infer that these potassium measurements are contaminated by the storage solution for the pH probe.

Table 3: pH and concentrations of Na, K and Ca in the outlet effluent.

Effluent No.	Sampling time [h] after experiment start	pH	Na [mmol/l]	K [mmol/l]	Ca [mmol/l]
1	27.67	-	75.84	1.01	-
2	45.22	-	80.15	0.75	1.26
3	50.50	7.46	87.44	34.79	1.08
4	73.48	-	84.44	0.73	3.03
5	104.08	6.98	80.81	17.67	2.82
6	140.68	-	82.76	0.52	5.46
7	150.75	7.2	81.50	4.79	6.24
8	165.35	-	81.73	0.44	6.10
9	172.50	7.01	80.83	6.07	6.16
10	196.52	-	78.20	0.58	5.99
11	217.80	7.09	80.35	6.45	6.93
12	242.62	7.1	81.95	4.73	6.75

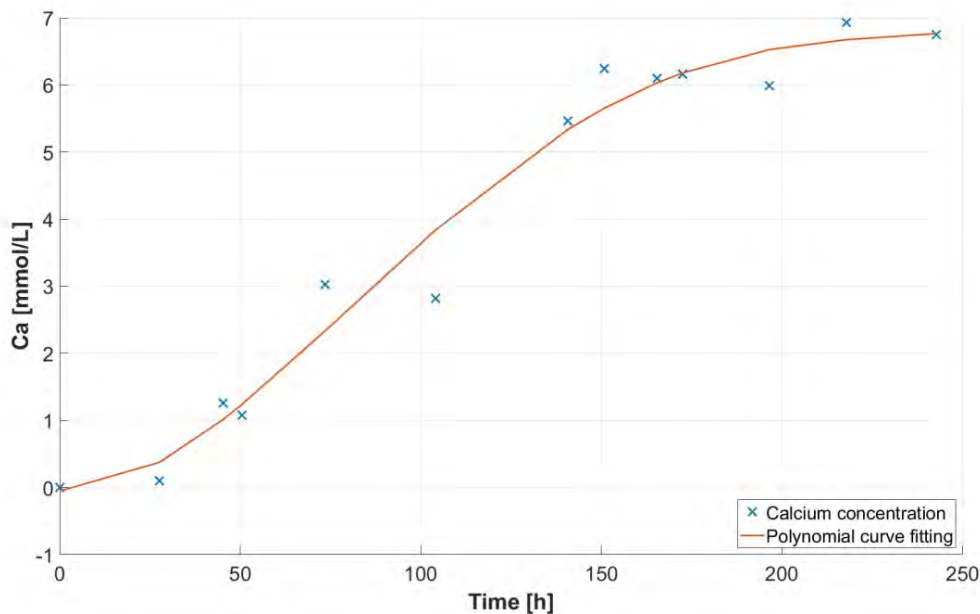


Figure 12: Evolution of calcium (Ca) concentration during the reactive flow through experiment on sample H4

The increase of Ca concentration (Fig. 12) indicates an increase in the dissolution rate or in the reactive surface area of calcite during the injection. The resulting accumulated volume of dissolved calcite is

shown in Figure 13; in total 0.022 ml has been dissolved. The solid volume of the core was re-measured after the experiment, using helium pycnometry. A loss of 0.032 ml in solid volume was detected, yielding a new porosity of 9.71%, and roughly balancing the volume of calcite that was dissolved.

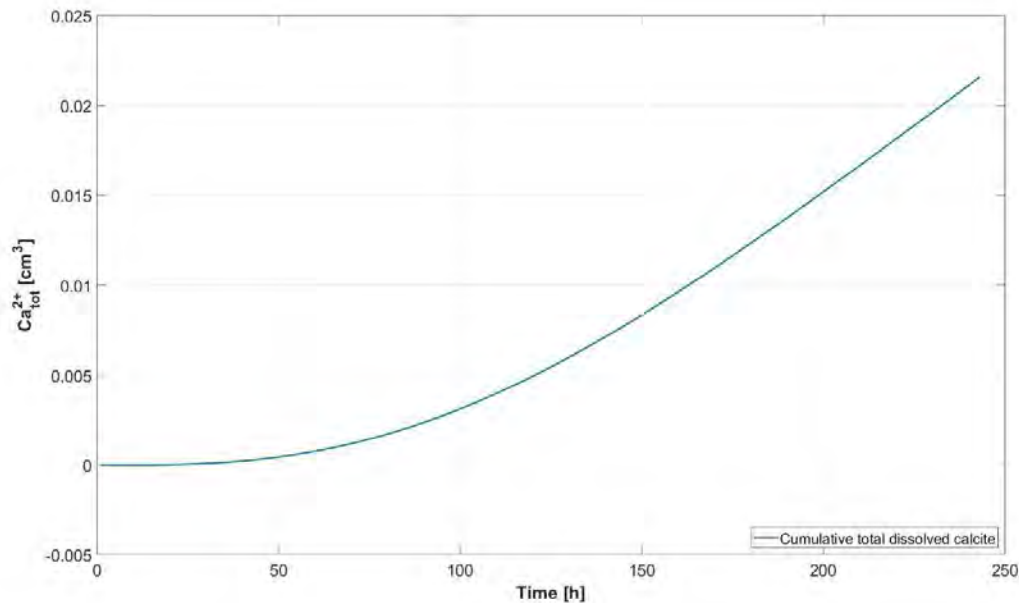


Figure 13: Cumulative dissolved calcium volume (cm³) for the reactive flow through experiment on sample H4

Sample H4 had a very low initial porosity of 9.39% and a low initial permeability of $1.72 \times 10^{-18} \text{ m}^2$, while sample H3 is of unconsolidated sandstone with a high porosity of 38.76%. Unexpectedly, the experiment to mimic the effect of acid stimulation on H4 did not increase its permeability. This might be because of the short duration of this experiment (~250 hours). Compaction and the release of fines might also have caused the decrease in permeability, obscuring the impact of the acid stimulation.

1.1.4.5 X-CT results

Figure 14A and B illustrate the pore space segmentation of the X-CT scan of sample H3, based on visual interpretation. Porosity was calculated for slices of this sample and varied from 17 to 20% (Figure 14C). Average porosity for the greyscale cut-off choice is 18%, its standard deviation being 0.6%. Layers of thickness 2-3 mm can be recognised with different porosity, presumably due to variations in grain size sorting. Porosity can be related to grain size sorting as highlighted by circles 1 and 2 in Figure 14B. In regions with lower porosity (circle 1), a larger range of grain size is recognised, whereby smaller grains reduce pore space. X-CT scans were also made for samples H1, H2 and H4. The porosity in these samples turned out to be very low, pore size being below the resolution of the scans. X-CT results are therefore only presented here for sample H3.

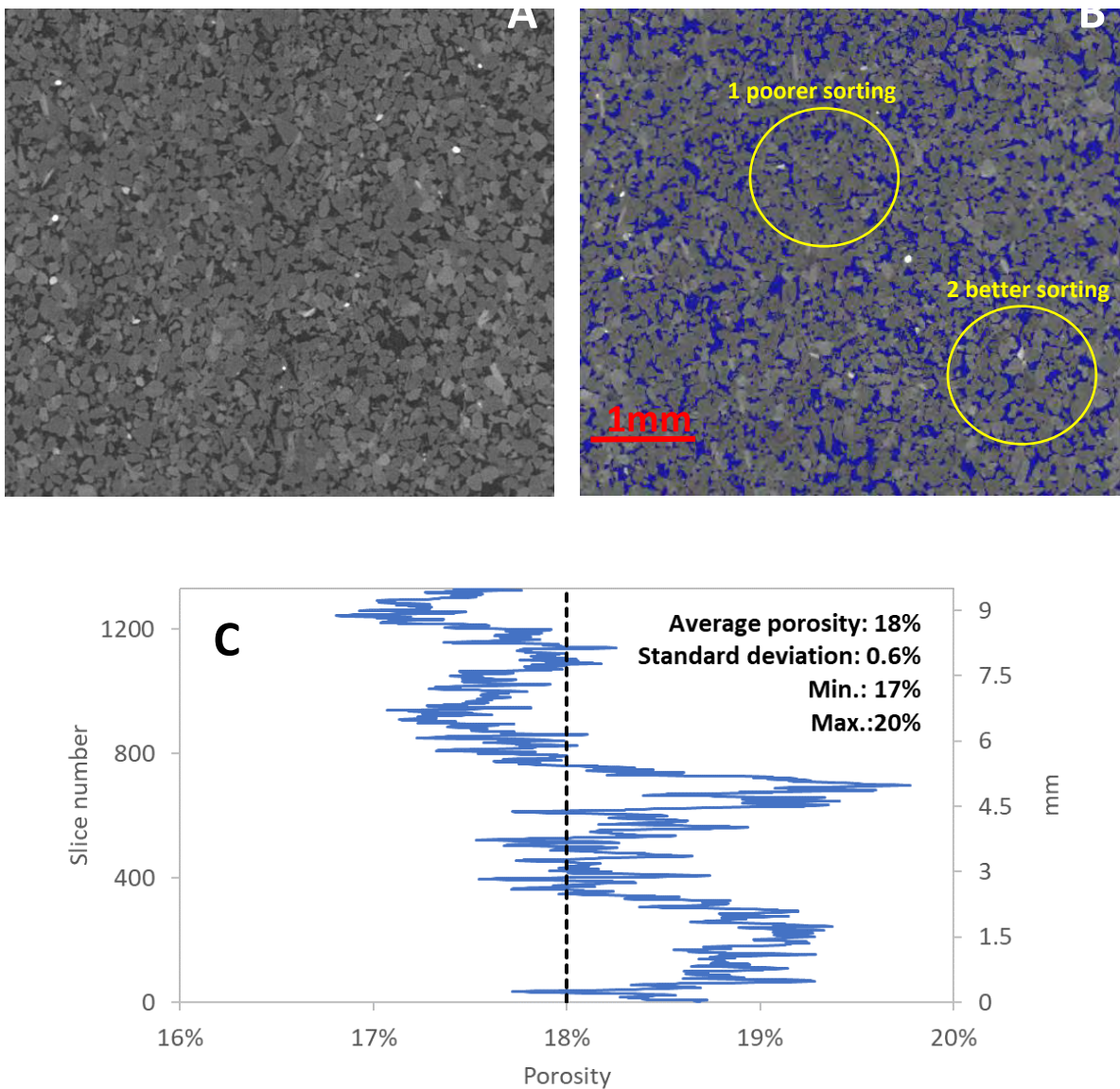


Figure 14: (A) and (B) XY plane of X-CT scan of sample H3 with variations in grain size sorting highlighted with yellow circles in B. (C) Porosity calculated for each XY slice of sample H3, indicating the range of values and the vertical trend across the sample.

1.1.4.6 Numerical flow through experiments

James Minto (Department of Civil & Environmental Engineering, Strathclyde University, Glasgow, UK), on behalf of the University of Glasgow participants in DESTRESS

Because the samples were too small for physical flow-through experiments, permeabilities of samples were calculated using a Digital Rock Physics approach applied to sub-volumes of the segmented X-CT scan data. Each sub-volume was a cube 1.43 mm (200 voxels) to a side (Figure 15B); 84 sub-volumes in total were modelled. Permeability was calculated independently for flow along the X, Y and Z axes (Figure 15C); this was repeated for three different segmentation thresholds applied to the greyscale X-CT data, resulting in 756 (84×3×3) simulations.

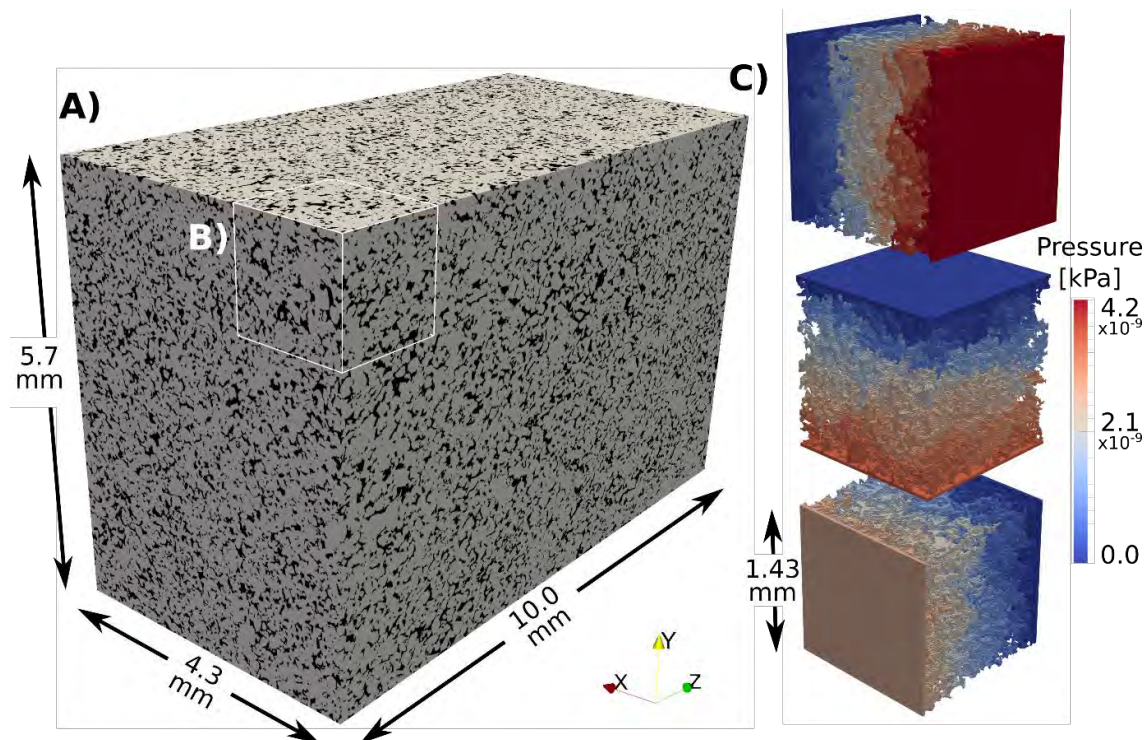


Figure 15: A) Section of X-ray CT scan segmented to show solids as grey, pore space as black. B) Sub-volume cube. C) Simulated pressure drop across a sub-volume calculated for flow parallel to the X, Y and Z axes.

The modelling software used was OpenFOAM v4.1 (openfoam.org). The solver used was simpleFoam which solves the Navier-Stokes equations for single-phase incompressible flow. Pore-scale geometry was created with the following steps:

1. Creation of hexahedral meshes for each sub-volume, where every mesh cell directly conformed to a voxel in the X-CT scan. Scan resolution was 7.147 μm and each sub-volume contained 8 million voxels hence the hexahedral meshes also contained 8 million voxels. All six sides of the bounding box were set as wall-type boundary patches named "Side".
2. Cells that contained a solid voxel were removed from the mesh leaving only pore space cells. Cell faces exposed by this operation were designated as wall-type boundary patches named "Walls".
3. Inlet and outlet boundary "plates" were added for flow distribution. These plates are analogous to the distribution plates used in rock core holders for experimental measurement of permeability. The boundary patches on these sides were modified to "Inlet" and "Outlet".
4. Regions of pore space not connected to the inlet and outlet plates (i.e. disconnected pore bodies) could not contribute to flow through the sub-volume and were removed.
5. Steps 3 and 4 were repeated for each axis.

Porosity was calculated at step 2 (total porosity) and at step 4, discounting the boundary plates (connected porosity).

Table 4. Boundary conditions for numerical flow-through experiments.

Boundary name	Type	Velocity field	Pressure field
Inlet	patch	fixed velocity	zero gradient
Outlet	patch	zero gradient	fixed pressure
Side	wall	slip	zero gradient
Walls	wall	no-slip	zero gradient

A constant flow velocity of 10^{-12} m/s into the model domain was specified on the inlet patch, and a fixed pressure of 0 kPa was specified at the outlet patch. Walls created when removing solid cells (step 2) were given a no-slip velocity boundary condition as they represent a solid surface at which velocity must be zero. Side walls were given a slip velocity boundary condition as they represent pore bodies which intersect the sub-volume bounding box. The full set of boundary conditions is listed in Table 4. No turbulence model was included, and the inlet flow velocity was set to a very low number to ensure flow remained within the laminar regime. The simpleFoam solver was run for each sub-volume, flow axis, and segmentation threshold value until convergence criteria were satisfied. At this point, the average pressure at the inlet was measured and used – together with the specified flow velocity, outlet pressure, fluid viscosity and dimensions of the sub-volume – in Darcy’s equation to calculate the permeability of that sub-volume.

Plotting total porosity against permeability (Figure 16), it is apparent that these parameters are correlated. It is also apparent that permeability is uniformly highest for flow along the Z axis, and generally slightly higher along the Y axis compared with the X axis.

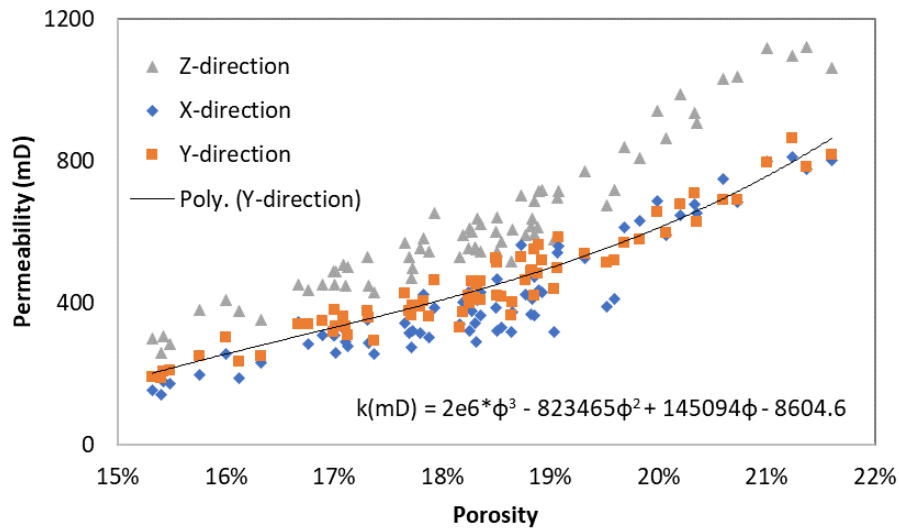


Figure 16: Total porosity and permeability for each sub-volume, flow direction (X, Y and Z) and the three segmentation threshold values.

As the segmentation threshold value increases, the resulting calculated permeability also increases. This is because porosity and pore connectivity increase, resulting in a greater capacity for flow through the pore network. Figure 17C and D show how the connected porosity has increased, resulting in lower flow velocities and fewer bottlenecks, whilst Figure 17A and B show how this translates into a lower pressure drop across the sub-volume and hence higher permeability.

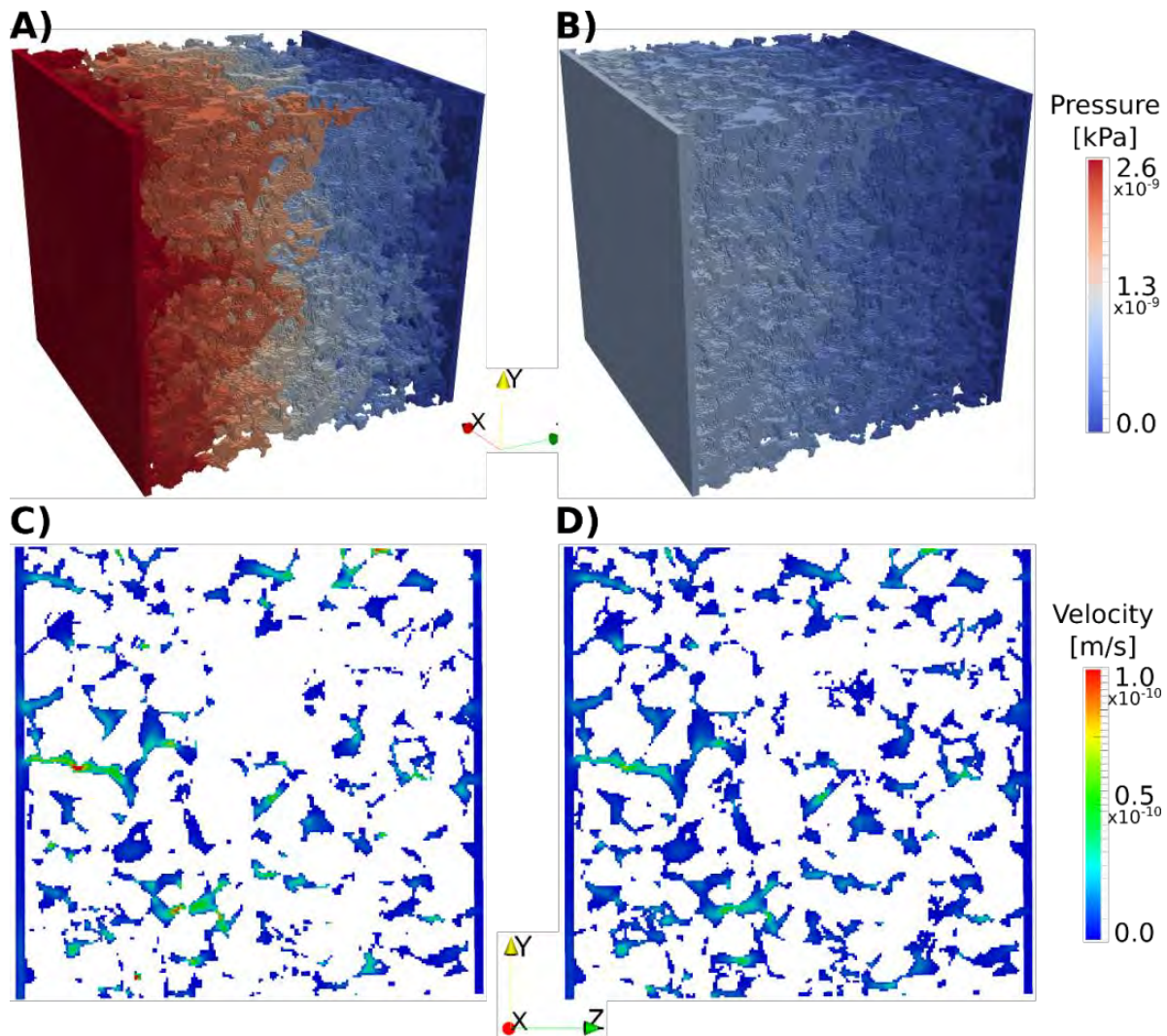


Figure 17: Pressure drops across a representative sub-volume for A) the mid segmentation threshold value of 7700, and B) the higher segmentation threshold of 8000. Velocity distributions within cross-sections through the sub-volume for C) the mid and D) the higher segmentation threshold.

References

- Andrä, H., Combaret, N., Dvorkin, J., Glatt, E., Han, J., Kabel, M., Zhan, X. (2013). Digital rock physics benchmarks-part II: Computing effective properties. *Computers and Geosciences*, 50, 33–43.
- Balint, A., M. Barcza, J. Szanyi, B. Kovacs, B. Kobor, T. Medgyes. (2010). Investigation of thermal water injection. In: 1st Knowbridge Conference on Renewables, 1–8. Miskolc, Hungary.
- Bando, S., Takemura, F., Nishio, M., Hihara, E., Akai, M. (2004). Viscosity of aqueous NaCl solutions with dissolved CO₂ at (30 to 60) °C and (10 to 20) MPa. *Journal of Chemical & Engineering Data*, 49, 1328-1332.
- Brooks, R.A., Di Chiro, G. (1976). Beam hardening in X-ray reconstructive tomography. *Physics in Medicine & Biology*, 21 (3), 390-398.
- Cnuddle, V., and Boone, M. N. (2013). High-resolution X-ray computed tomography in geosciences: a review of the current technology and applications. *Earth-Science Reviews*, 123, 1-17.
- Csato, I., Kendall, C.G.S., Moore, P.D. (2007). The Messinian problem in the Pannonian Basin, eastern Hungary - insights from stratigraphic simulations. *Sedimentary Geology* 201, 111–140.

- ENRES, 2011. ENRES Stratigraphic methods and workflow approaches in subsurface well correlations, accessed: 20/02/2020.
- Guibert, R., Nazarova, M., Horgue, P., Hamon, G., Creux, P., Debenest, G. (2015). Computational Permeability Determination from pore-scale imaging: Sample size, mesh and method sensitivities. *Transport in Porous Media*, 107, 641–656.
- Ketcham, R.A., Carlson, W.D. (2001). Acquisition, optimization and interpretation of X-ray computed tomographic imagery: applications to the geosciences. *Computers & Geosciences*, 27, 381-400.
- Mavko, G., Nur, A. (1997). The effect of a percolation threshold in the Kozeny-Carman relation. *Geophysics*, 62, 1480–1482.
- Marshall, T. (1958). A relation between permeability and size distribution of pores. *Journal of Soil Science*, 9 (1), 1-8.
- Nador, A., Kujbus, A., Toth, A.N. (2016). Geothermal energy use, country update for Hungary. European Geothermal Congress 2016, Strasbourg, France.
- Noiriél, C. (2015). Resolving time-dependent evolution of pore-scale structure, permeability and reactivity using X-ray microtomography. *Reviews in Mineralogy and Geochemistry*, 80, 247-285.
- Olariu, C., Krezsek, C., Jipa, D.C. (2018). The Danube River inception: Evidence for a 4 Ma continental-scale river born from segmented Paratethys Basins. *Terra Nova*, 30, 63–71.
- Szanyi, J., Kovács, B. (2010). Utilization of geothermal systems in south-east Hungary. *Geothermics*, 39, 357–364.
- Sztanó, O., Szafián, P., Magyar, I., Horányi, A., Bada, G., Hughes, D.W., Hoyer, D.L., Wallis, R.J. (2013). Aggradation and progradation controlled clinothems and deep-water sand delivery model in the Neogene Lake Pannon, Makó Trough, Pannonian Basin, SE Hungary. *Global and Planetary Change* 103, 149–167.
- Toth, A.N. (2015). Hungarian country update 2010-2014. World Geothermal Congress 2015, Melbourne, Australia.
- Verri, I., Della Torre, A., Montenegro, G., Onorati, A., Duca, S., Mora, C. A., Trombin, G. (2017). Development of a Digital Rock Physics workflow for the analysis of sandstones and tight rocks. *Journal of Petroleum Science and Engineering*, 156, 790–800. h

Acknowledgements

We thank the staff of the Advanced Materials Research Laboratory (AMRL) of Strathclyde University for their assistance, especially Alice Macente for the X-ray Computed Tomography analysis and Tiziana Marocco and Fiona Sillars for the thermal property analysis. We also thank Object Research Systems for granting an academic license for their Dragonfly image analysis software and Panterra Geoconsultants for granting an academic license for their Cyclolog ENRES INPEFA software.

1.2 Westland, the Netherlands

Jan Ter Heege

The experimental work on core samples from the Westland site is described in detail in Deliverable 4.2. Only a summary of the key aspects is provided here. The report for DESTRESS Deliverable 4.2 includes (1) a short review of the theory underpinning subcritical crack growth, (2) an analysis of typical experimental data for subcritical fracture growth velocities in sandstones, and (3) an analysis of hydro-mechanical properties of the tight Triassic sandstone targeted by the Trias Westland project in the Netherlands. Core samples that were retrieved of these reservoir rocks nevertheless provided a unique opportunity to further study the effect of potential stimulation, including the effect of subcritical crack growth on permeability and strength.

This experimental work aimed to explore methods to determine the contribution of subcritical crack growth to permeability increase in the tight Triassic sandstone reservoir in the Netherlands, using core samples recovered from the Trias Westland well. Subcritical fracturing can contribute to stimulation of permeability as it is observed to reduce formation breakdown pressure and to enlarge the zone disturbed by fracturing. It may contribute to more efficient, low risk stimulation of reservoir permeability by (1) reduction of injection rates and volumes required for stimulation, (2) better optimization of stimulation, and (3) progressively increasing permeability and flow rates during operation of geothermal doublets. The experiments focussed on determining hydro-mechanical properties of the tight sandstone reservoir rock, a major goal being to obtain information on saturation and poroelastic properties of the sandstone. The samples were deformed in axial compression to determine Young's modulus as well as failure and residual strength. Outcomes of the experiments confirmed the low permeability found in the well tests and previous core analysis. It was also found that (1) poroelastic stressing does not indicate effects of increasing saturation and (2) the Darcy flow test does not indicate any flow across the sample.

The measured properties of the Triassic sandstone targeted by the Trias Westland project indicate that this reservoir is much too tight to be considered for geothermal energy. Core analysis showed helium porosity values of 1.4-3.9% and Klinkenberg permeability below 0.02 mD. Flow rates will therefore be negligible unless the low reservoir permeability is restricted to the near well area or high permeability zones exist that can be connected to wells by stimulation. The site developer therefore cancelled the pre-existing plans for stimulation, withdrew from the DESTRESS project, and decided to pursue exploitation of a shallower Cretaceous reservoir.

1.3 Klaipėda, Lithuania

Sean Watson, Rob Westaway, Neil Burnside, Nicolas Beaudoin, Jin Ma, Xiang-Zhao Kong, Martin O. Saar

1.3.1 Geological overview

Lithuania contains a varied geological sequence comprising of a largely continental sedimentary sequence which dips and thickens towards the north-west, overlying metamorphic and metasedimentary basement rocks of the Pre-Cambrian Baltic Shield (e.g., Brehme et al., 2019). Potential geothermal resources have been identified in three stratigraphic horizons: (i) the Upper-Middle Devonian Šventoji (D₃) – Upninkai (D₂) complex; (ii) the Middle – Lower Devonian Parnu-Kemeri-Gargždai (D₂-D₃) complex; and (iii) the Cambrian Deimena – Kybartai – Gegė – Virbalis strata (Brehme et al., 2019). Of relevance to the present study, the Upper Devonian (D₃-D₂) complex comprises the Šventoji and Upninkai Formations which are composed of sands and poorly cemented sandstones, silts, clays and some dolomitic marls (Brehme et al., 2019). The Middle to Lower Devonian Kemeri Formation comprises friable sandstones with interlayers of strongly cemented sandstones. These interlayers are cemented by clay, carbonates, gypsum and quartz, with siltstone and shale interlayers (Zinevicius et al., 2020). The rocks that form the geothermal reservoir at Klaipėda are designated the Viešvile Formation of Early Devonian age, this being a sub-unit within the Kemeri Formation. The Devonian age formations present in the subsurface at Klaipėda become progressively shallower moving eastwards across Lithuania and northeastwards into neighbouring Latvia.

At the time when these rocks were deposited, Lithuania was located at subtropical latitudes in the southern hemisphere near the SE margin of the ancient continent of Laurussia. As a result of earlier motions of tectonic plates, Laurussia was transected by the Caledonian mountain range, erosion of which provided the source of the widespread sandy sediments deposited at this time. The Earth's climate at the time is not yet fully understood, but it is thought (e.g., Kiipli et al., 2016) that along the SE margin of Laurussia aridity was interspersed with moisture as a result of monsoon systems originating in the ocean located to the southeast. Rocks in the Baltic region, dating from this time, thus consist not only of sandstone, the product of erosion of the Caledonian mountains, but also abundant clay minerals, the product of chemical weathering of rocks, indicating a subtropical environment (e.g., Kiipli et al., 2016). There is a possibility therefore that the blockage of flow in the Klaipėda geothermal project might be a consequence of pervasive clay minerals clogging pore space within the sandstone. On the other hand, it is possible that the cause relates to chemical precipitation as a result of changes in the temperature and pressure in the circulating fluid. Conceivably a combination of mechanisms, including these, might be in operation. Another potential mechanism for making the Viešvile Formation sandstone beneath Klaipėda relatively impermeable is the presence of calcium carbonate cement between sand grains (Pipira et al., 2015). Such cementation might be expected as a result of evaporation of groundwater shortly after deposition, thus indicating warmth and aridity in the palaeoclimate.

1.3.2 Fieldwork sample acquisition

Following a literature review, dialogue with local specialists and consultation of large-scale geological maps, localities where outcrop analogues of the Klaipėda reservoir rocks were identified. Fieldwork was conducted in April 2017, to visit localities in Lithuania and Latvia to collect samples from Devonian sandstone outcrops. Core samples of the Viešvile Formation were also obtained, from the Palanga-318a and Vydmantai-1 boreholes, stored at the Vievis core archive near Vilnius, Lithuania. In addition, a core sample of the Viešvile Formation from the Klaipėda-1I well was obtained from the Klaipėda geothermal project operator, Geoterma. The Vydmantai-1 and Palanga-318a wells are located ~30 km north of the Klaipėda geothermal site; given the low lithological and petrophysical lateral variability of the sandstone reservoir, the cored successions are considered analogous with the Viešvile Formation

encountered at Klaipeda. Both these boreholes encountered strata that consist of fine-grained sandstone, dolomite, clay and gypsum. Overall, 19 samples of borehole core and 13 outcrop samples were collected (Tables 5 and 6). A more detailed description of this fieldwork can be found in DESTRESS Deliverable 6.1. The outcrop samples were collected in two areas: from exposures in river cliffs along the River Gauja and its tributary, the Amata, in central Latvia; and from cliffs on the Baltic coast not far south of the border with Estonia.

Table 5: Core Samples

Name	Formation	Borehole	Depth (m)
KLA 1I	Viešvile Formation	Klaipeda 1I	1107.4
PAL 918	Viešvile Formation	Palanga 318a	918
PAL 937	Viešvile Formation	Palanga 318a	937
VYD 984	Viešvile Formation	Vydmantai 1	984
VYD 987.6	Viešvile Formation	Vydmantai 1	987.6

Table 6: Outcrop Samples

Name	Formation	UTM Coordinates	Location
A1	Amata Formation	35V 0387640 6348009	River Amata
E1	Amata Formation	35V 0395422 6358937	Erglu Cliffs on the River Gauja, Cesis
V1	Burtnieki Formation	35V 0342662 6385349	Veczemji Cliffs, Tūja, Baltic coast
Z1	Amata Formation	35V 0392750 6343793	Zhiguli Cliffs on the River Amata, Melturi

1.3.3 X-CT Methodology

Recapping from subsection 1.1, X-Ray Computed Tomography (X-CT) is a non-destructive and non-invasive method which uses contrasts of X-ray attenuation (a function of density and atomic number) to reconstruct the 3D distribution of areas of different densities within a large variety of materials. The 3D reconstruction is based on a series of contiguous 2D radiographs taken with different view angles, rotating a sample around a single axis in small steps. X-CT has been increasingly used in Earth Science over the past two decades (Ketcham and Carlson, 2001; Cnudde and Boone, 2013). Amongst many other examples, X-CT analysis has been successfully utilised to unravel the shape, orientation and 3D distribution of minerals, porosity and cracks in sedimentary rocks (e.g., Noiriél, 2015).

The X-CT scans were performed using a Nikon XTH 320/225 system at the Advanced Materials Research Laboratory at Strathclyde University. This facility is funded by the Scottish Government Oil and Gas Innovation Centre (OGIC) and shared between University of Glasgow and Strathclyde University. The system is equipped with a 225-kV reflection gun and a 2000 × 2000-pixel flat panel photodetector (cell size 0.2 × 0.2 mm). No filters were used for the scans.

The first sample to be scanned was KLA 1I. This sample was scanned in its original state given the request by the site operator to preserve core material from this borehole. Given the size of this sample the scanned voxel size (resolution) was 31.66 µm. The exposure time for each projection was 708 ms, the scan lasting for 1600 projections.

For the remainder of the scanned samples it was possible to prepare a small chip of the core or outcrop material. This allowed for an improved scan resolution, enabling smaller pores to be observed. For

these samples, the exposure time for each projection was 2829 ms, the scan again lasting for 1600 projections. The X-ray source to sample distance was set to achieve an approximate minimal voxel size of 3.5-5 μm . The accelerating voltage and current of the X-ray source varied depending on the target voxel size. Scanning conditions are summarised in Tables 7 and 8.

Table 5: X-CT Operational Details for Borehole Samples

Name	Resolution (μm)	Scan Size (μm)	Voltage (kV)	Current (μA)
KLA 1I	31.66	-	170	28
PAL 918	3.50	4109.27 x 2881.73 x 5441.72	145	21
PAL 937	3.50	4343.58 x 4493.97 x 5403.25	145	21
VYD 984	3.50	3210.48 x 3934.41 x 5452.21	145	21
VYD 987.6	3.50	2748.84 x 4347.08 x 5329.81	145	21

Table 6: X-CT Operational Details for Outcrop Samples

Name	Resolution (μm)	Scan Size (μm)	Voltage (kV)	Current (μA)
A1	4.50	2755 x 3502.27 x 2358.85	159	25
E1	5.00	6999 x 5499.92 x 6999.9	110	41
V1	4.50	5401.91 x 6752.39 x 6752.39	159	25
Z1	5.00	4219.97 x 5464.97 x 5759.97	110	41

To ensure accurate quantitative results it is necessary to have high quality images, which avoid sources of error such as artefacts due to the image reconstruction process. 3D volumes were reconstructed from projections using the CT Pro 3D software (© 2004-2016 Nikon Metrology), with an automatic reconstruction tool to find the centre of rotation of the scan and applying a beam hardening correction (Brooks and Dichiro, 1976). Ring artefacts, which are common in micro X-CT, affected the segmentation process, although this was mitigated by removing the slices affected. All volumes were reconstructed in 16 bits (65536 grey values).

To reconstruct the surfaces of the samples, the 3D volumes were processed using Avizo (v.9.2.0, © FEI), for the KLA 1I sample, and Dragonfly (v. 4.1.0.647, © Object Research Systems (ORS) Inc.), for the remainder of the samples. The following image processing analysis was performed in both software packages.

First, the noise was reduced by applying an edge-preserving smoothing filter (“bilateral filter”) that averages the intensity value of a voxel with regard to that of its neighbours, considering the neighbours defined by a $3 \times 3 \times 3$ kernel size. To reduce the effect of ring artefacts and beam hardening at the edges of each sample, a sub-volume within the sample was created using the “crop” tool. This allowed mitigation of the aforementioned effects as well as limiting the opportunity to segment external air, and instead only focusing on the internal pore space. Each phase (mineral and pore) were separated manually using simple greyscale thresholding, by segmentation of the volumes corresponding to the relative density range of each individual phase. Segmentation is considered optimal when the selected range of grey values selects all the voxels belonging to the pore phase, avoiding voxels that belong to the mineral phase. Such optimal separation is achieved with a strong contrast between the phases. Pixels attributed to noise were then removed using the “remove small spot” function, which consists of deleting all clusters of <10 pixels from the segmented 3D data. The volumes of the mineral phase

and pore phases were then determined by the software packages by “counting” the voxels in the respective voxel clusters. The choice of grey scale value used to segment the pores and the mineral phases influences the resulting value of porosity within the sample volume. To achieve the optimal value, a sensitivity analysis was conducted using numerous grey scale values to represent the segmented pore space.

1.3.4 X-CT Results

For each sample, a range of porosity is given based upon the segmentation sensitivity analysis. A porosity value adjudged to be the most representative of the sample scan is also shown. A more detailed description of the experimental work on the Klaipeda samples can be found in DESTRESS Deliverable 6.1.

Table 7: X-CT Porosity Results

Name	Formation	Depth (m)	Porosity (%)	Porosity Range (%)
KLA 1I	Viešvile Formation	1107.4	8.40	-
PAL 918	Viešvile Formation	918	18.05	16.94-20.33
PAL 937	Viešvile Formation	937	22.23	19.52-24.58
VYD 984	Viešvile Formation	984	9.60	5.96-14.77
VYD 987.6	Viešvile Formation	987.6	3.11	2.55-3.83
A1	Amata Formation	Outcrop	25.34	21.06-28.66
E1	Amata Formation	Outcrop	23.38	22.01-24.77
V1	Burtnieki Formation	Outcrop	28.01	14.44-36.03
Z1	Amata Formation	Outcrop	7.93	5.88-10.43

1.3.5 Discussion and Conclusion on X-CT analysis

The aims of this work were to determine using X-CT analysis the porosity of samples and to provide an insight into the possible presence of pervasive clay minerals or carbonate cement blocking pore space within the samples. While the X-CT analysis can provide an indication of the porosity of each sample and show that different mineral phases are present, it must be paired with further petrophysical and mineralogical analysis to determine the mineral composition of each sample. Nonetheless, this work provides an initial indication of the porosity and the mineralogical properties of the samples. The measurements show that the porosity within the Devonian sandstones in the Baltic region is higher at outcrop than at reservoir conditions in the Klaipeda-1I and Vydmantai-1 wells. However, the samples obtained from the Palanga-318a well show a greater similarity to those at outcrop and indicate less influence of cementation or clogging of pores with pervasive clay minerals. The X-CT scans show that the Klaipeda-1I well has a porosity of ~8.4%, with evidence of cementation and different mineral phases shown. This value of porosity is influenced by the scanning conditions and the size of the core sample and therefore should be considered as a conservative estimate. The Vydmantai-1 samples are well cemented, initial estimates of porosity being 3.11% and 9.60%. X-CT scans show evidence of abundant carbonate cement and that porosity is fracture dominated. However, these fractures are likely to be a result of sample preparation and are not representative of reservoir conditions, therefore these porosity values can be inferred to be optimistic. The Palanga-318a samples have estimated porosities of 18% and 22%, with less cementation and consolidation evident, although some carbonate cement is observed.

The outcrop samples are much less consolidated and have greater porosity than the borehole core samples, porosity ranging from 23-28% for the Amata and Burtnieki formations (samples A1, E1, and V1). These samples are similar in porosity and mineralogical composition, indicated by similar mineral phases evident in the X-CT scans. Sample Z1, of the Amata Formation, has a lower porosity, ~8%, and higher cementation compared with the other outcrop samples. This sample was observed at outcrop as being fine grained sandstone diagenetically altered with greater carbonate cement content. There is a greater similarity between this sample and those from reservoir conditions in the Viešvile Formation in the Klaipeda-1I and Vydmantai-1 wells. This work indicates the importance of studying outcrop and core material from analogous Devonian sandstone formations to provide an insight to reservoir conditions at the Klaipeda geothermal site. The relationship between porosity, permeability and mineralogy can be assessed further by investigating the mineralogical composition of the samples.

1.3.6 Mineralogy, porosity and flow-through experiments

Sandstone samples have been collected from borehole Vydmantai-1 at 954.6 m depth and borehole Palanga-318a at 981 m depth. Sample porosities have been measured in the Rock Deformation Laboratory at ETH Zurich, yielding a porosity of 21.9% for the Vydmantai sample and 8.76% for the Palanga sample. The bulk rock densities were measured as 2.11 g/cm³ for the Vydmantai and 2.52 g/cm³ for the Palanga sample. The compositions of both samples are listed in Table 8. Mineralogical analyses suggest that dolomite is the most reactive mineral in both samples in an acidic environment.

Table 8 Sandstone compositions

Vydmantai sample		Palanga sample	
Mineral	Fraction (wt. %)	Mineral	Fraction (wt. %)
Quartz	58.38	Quartz	50.38
Dolomite	15.78	Dolomite	36.60
K-feldspar	11.15	K-feldspar	5.92
Muscovite	6.07	Muscovite	2.74
Kaolinite	7.93	Kaolinite	2.33
Ilmenite	0.69	Illite	2.02

A first reactive transport flow-through experiment was performed on the sandstone sample from the Vydmantai-1 borehole in the geothermal lab of ETH Zürich (see Figure 18 for a system diagram). The experiment was conducted at a temperature of 40 °C, an outlet pressure of 100 bar and a confining pressure of 200 bar, similar to the reservoir conditions. A solution of 1 mol/l NaCl with 0.8 mol/l CO₂ was re-cycled through the sample for 10 days, with a total of 137 cycles, at flow rates of 2 ml/min for the first 42 cycles and 1 ml/min for the rest.

In-situ bulk permeability of sample was evaluated using the recorded differential pressure across it. The circulating fluid was sampled at both the inlet and the outlet of the reaction cell during the experiment. In addition, the pre- and post-experiment bulk permeabilities were also examined, employing the 1 mol/l NaCl brine at the same pressure and temperature (Figure 19). The bulk permeability of the sample steadily decreased from 356 mD before the experiment to 139 mD after it. During the period at a flow rate of 2 ml/min, the bulk permeability declined quickly at the start, then seems to have remained roughly constant from 40 to 66 hours. Immediately after the reduction in the

flow rate from 2 to 1 ml/min, the bulk permeability declined sharply over 5 hours, then stabilized again for the rest of the experiment. The reduction of bulk permeability as dolomite ($\text{Ca}_{1.05}\text{Mg}_{0.75}\text{Fe}_{0.2}(\text{CO}_3)_2$) cement dissolved may have been caused by the release of fine particles that subsequently migrate and clog fluid flow paths. In contrast to the decrease in permeability, sample porosity increased from 21.9% to 23.2% due to a solid volume loss of 0.25 ml during the experiment.

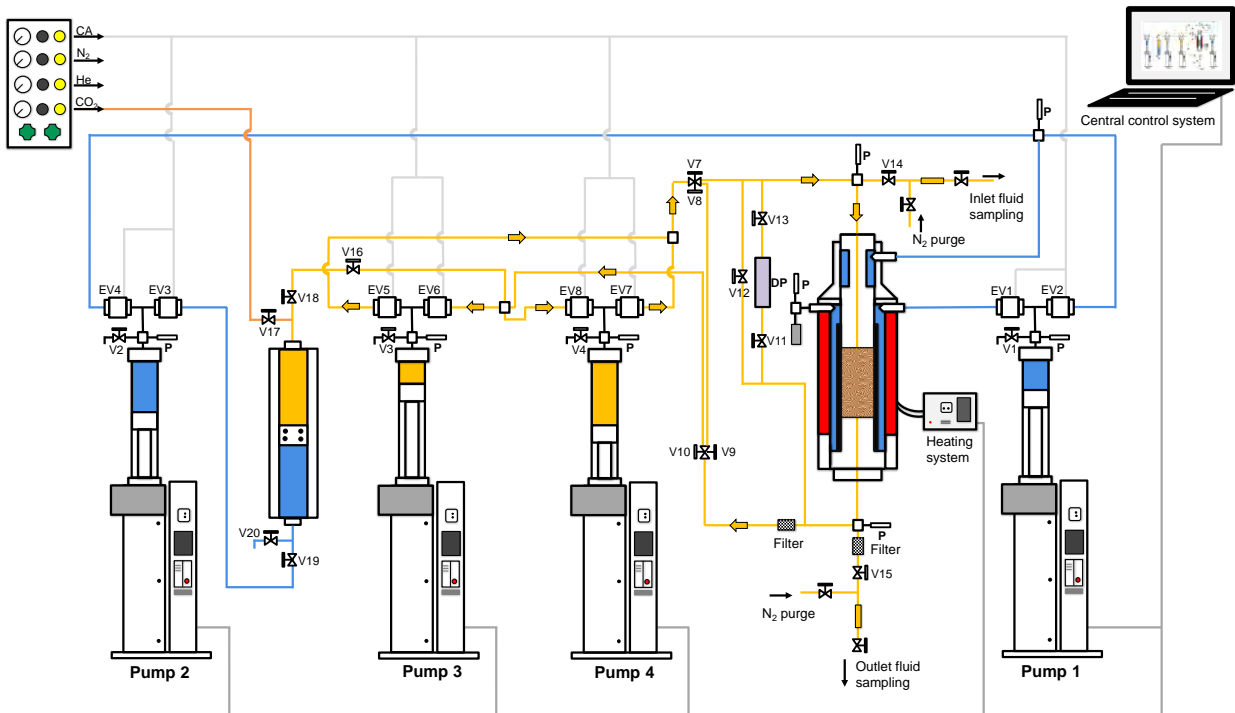


Figure 18: Sketch of the flow-through experiment.

Three-dimensional X-CT images of this sample have been produced at a resolution of $10.3 \mu\text{m}$, before and after the flow-through experiment. A mean grey scale variation of $\leq 2\%$ can be observed for the same mineral in the X-CT images, even though the two X-CT scans were conducted using identical settings. The pore fraction and the average grey scale of solid were calculated using the two sets of 3D X-CT images, as an indication of dolomite dissolution. As is shown in Figure 19, as a result of the experiment, the average grey scale of the X-CT image decreased by $\sim 3\%$, indicating a reduction of high-density mineral content (in this case, dolomite) and a $\sim 2\%$ increase of porosity, especially near the inlet end of the sample.

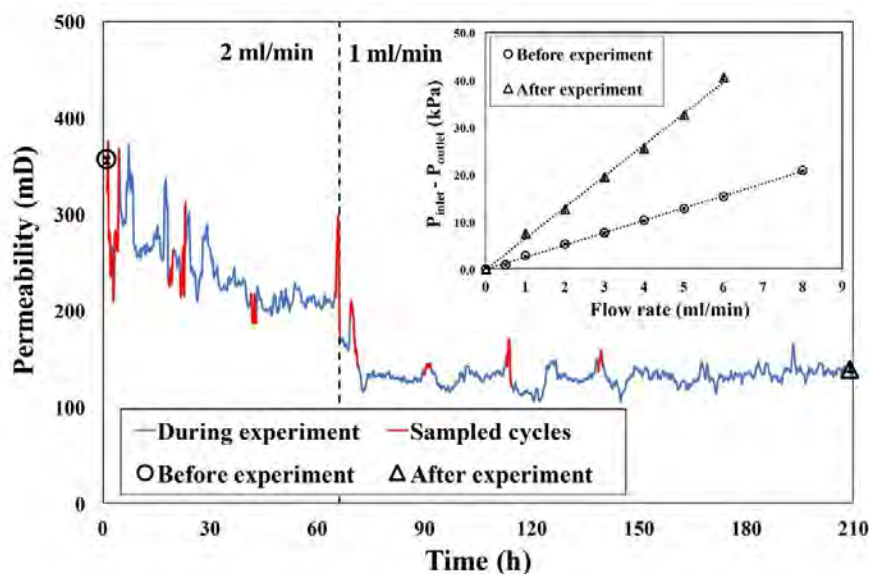


Figure 19: Permeability before, during and after the flow-through experiment.

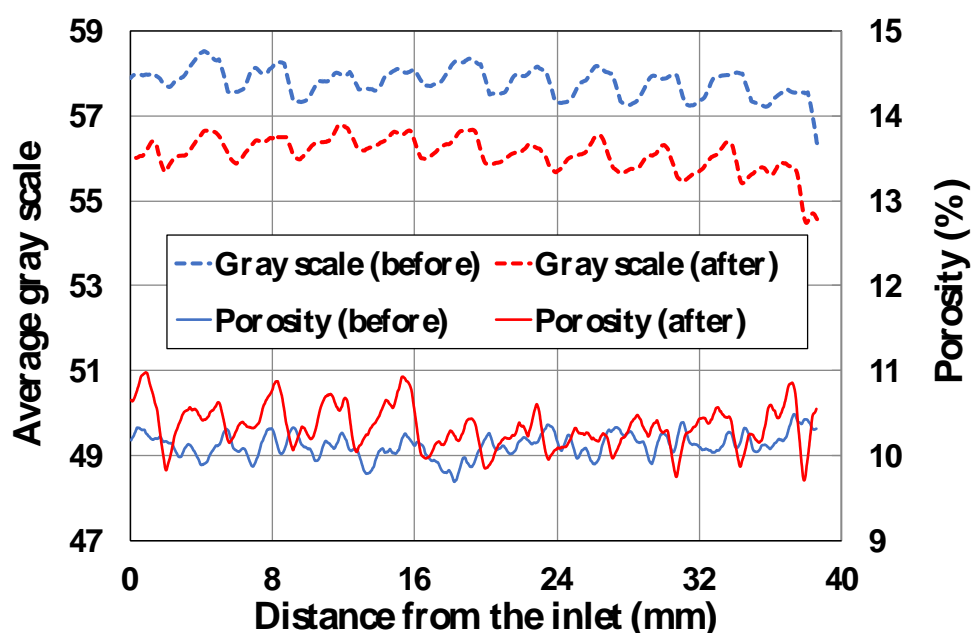


Figure 20: Average grey scale (dashed lines) of solids/minerals and porosity (solid lines) along the sandstone specimen before (in blue) and after (in red) the flow-through experiment, calculated from the X-CT images (at a resolution of $10.3 \mu\text{m}$).

The collected fluid samples were analysed using ICP-OES to infer mineral-fluid reactions. Major cations identified in these fluid samples include calcium, magnesium, iron, potassium, and aluminium. From the chemical analysis, dolomite reactivity and the corresponding effective surface area (ESA) are determined during the experiment (Figure 21 and Figure 22). The calculated dolomite reactivity decreased monotonically over time from $2.45 \text{ mmol m}^{-3} \text{ s}^{-1}$, abrupt reductions being observed during the fluid circulation at 2 ml/min along with more gradual reductions during the circulation at 1 ml/min. Comparing the ESA at the beginning of the experiment to the accessible surface area, which was obtained from SEM image analysis ($0.065 \text{ m}^2/\text{g}$, for details see DESTRESS deliverable 6.1), a surface effective coefficient $e = 1.36 \times 10^{-2}$ can be determined. The small value of e , of $\sim 1\%$, indicates a

highly limited participation of the total dolomite surface area that is exposed to the dissolution reaction.

To further examine the evolution of ESA during dolomite dissolution, a simplified, image-based numerical model was developed, employing a stochastic Monte-Carlo approach. This model takes the SEM image as its input, for which only dolomite is set as the reactive mineral phase. With this model, 100 stochastic Monte-Carlo realizations were conducted with a surface effective coefficient of $e \approx 1\%$. The changes in dolomite volume and ESA were recorded for each dissolution realization (Figure 203). Figure 24 demonstrates a satisfactory agreement between the simulation and the experimental observations, with respect to the relationship between the ESA and the dissolved dolomite volume. This work provides a potential approach to estimate the ESA evolution of reactive phases in a multi-mineral system when an up-scaling ESA factor is needed.

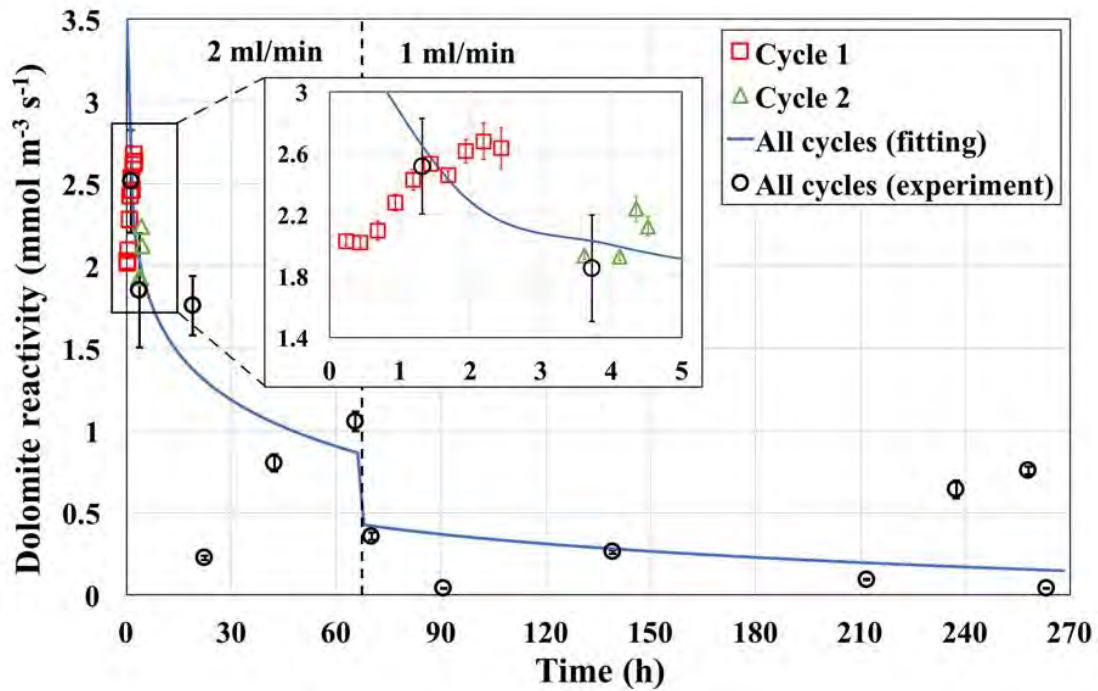


Figure 21: Evolution of dolomite reactivity (with an enlargement for the first two cycles) calculated with Ca concentrations.

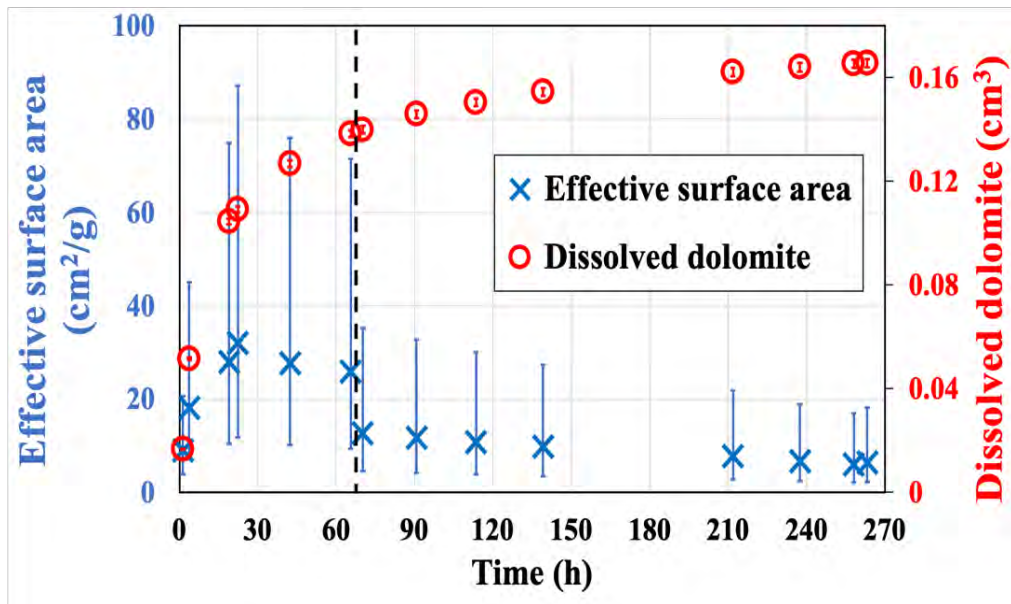


Figure 22: Evolution of the ESA (blue cross) and the dissolved volume (red open circle) of dolomite.

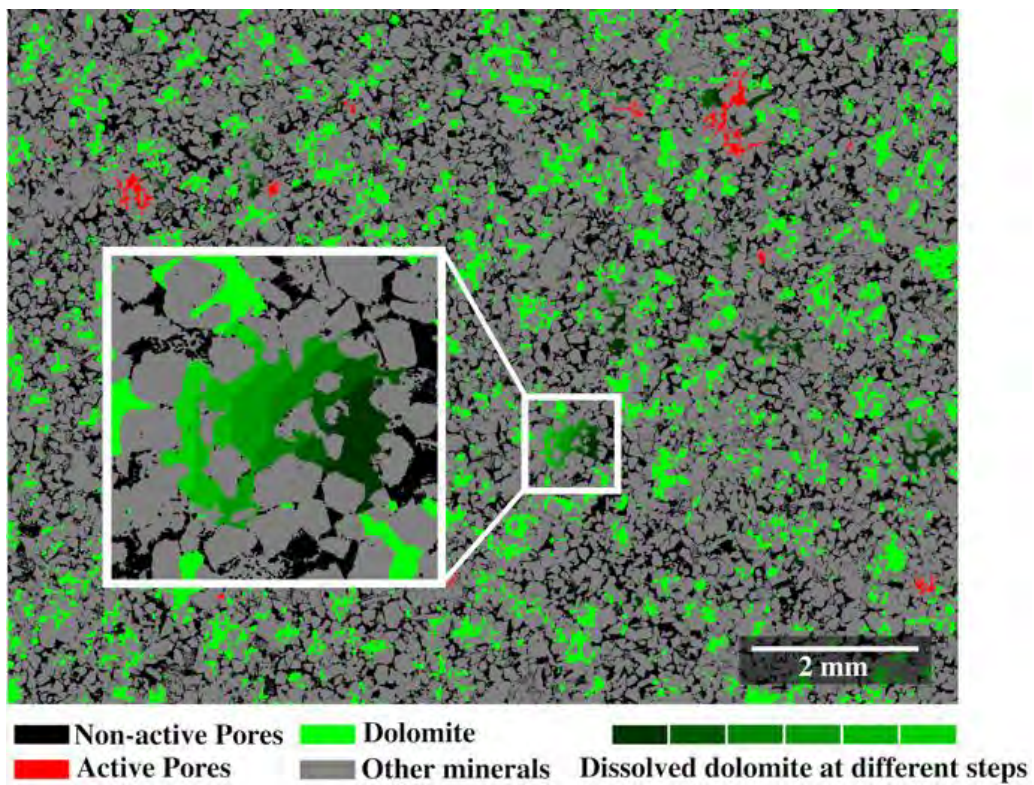


Figure 23: Image-based stochastic dissolution simulations, showing the evolution of the dolomite dissolution pattern in the SEM-EDS image.

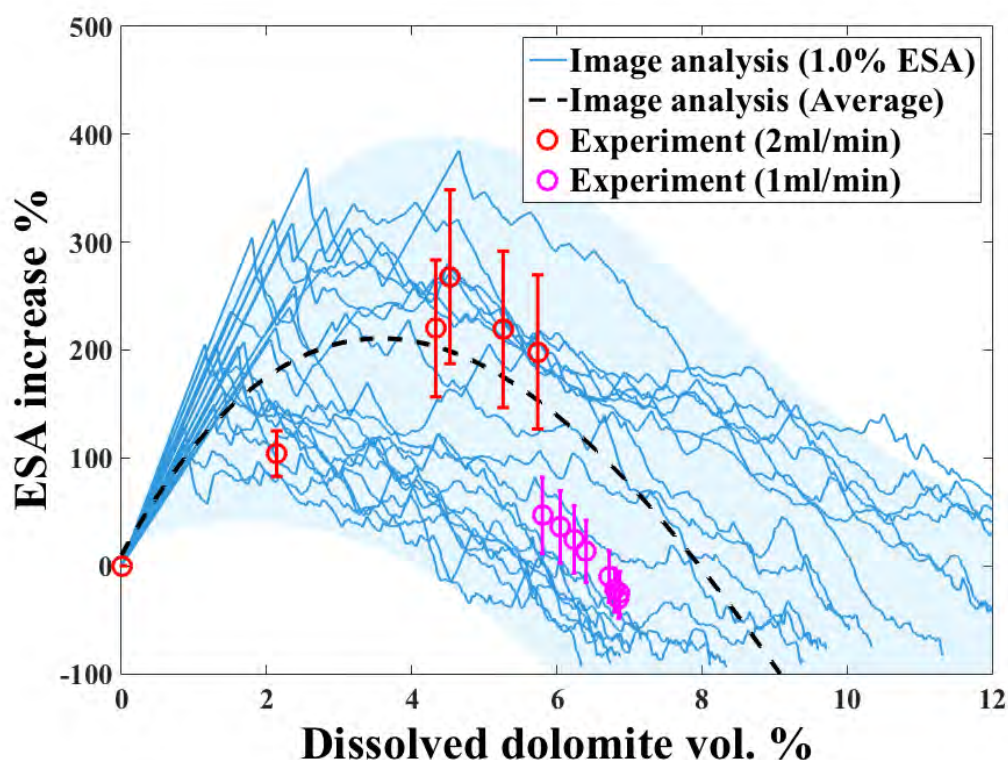


Figure 24: Relationship between the relative increase in dissolved dolomite volume and that of the ESA.

A second reactive flow-through transport experiment has been performed on a sandstone sample from the Palanga-318a borehole, to examine the geochemical reaction effects on rock mechanical and hydraulic properties. This experiment included three steps: (1) pre-acid stimulation; (2) acid stimulation; and (3) post-acid stimulation. During step (1), a series of experiments at reservoir conditions was performed to investigate the effects of effective stress, confining pressure, and pore pressure on the bulk permeability of the sample. The pressure loading path is shown in Figure 25. During step (2), a 3-week reactive flow-through experiment at reservoir conditions (with pore pressure 100 bar, confining pressure 200 bar and temperature 40°C) was performed, right after the step (1), using acid (CO₂-enriched brine) injection, to examine the effects of geochemical reactions on the bulk permeability of the sample. During step (3), like step (1), a series of experiments at reservoir conditions was performed to investigate the effects of effective stress, confining pressure, and pore pressure on the bulk permeability after acid stimulation. Fluid samples were collected during step (2) and analyzed using ICP-OES to infer mineral reactions. Porosity of the sample was also measured before and after the reaction, using helium pycnometry. An increase of porosity from 8.76% to 9.73% was observed due to mineral dissolution.

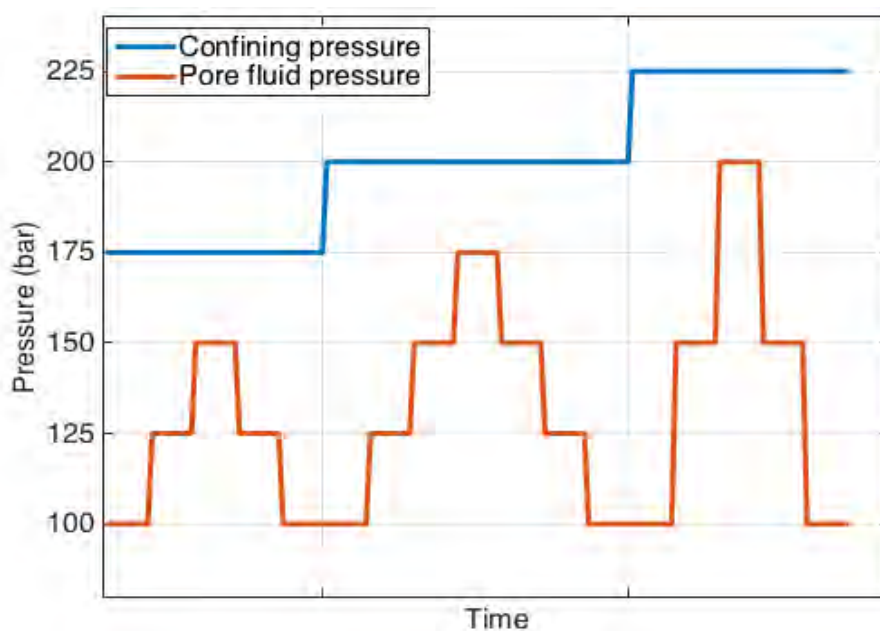


Figure 25: Loading path of confining and pore fluid pressures during the permeability tests before and after the acid simulation.

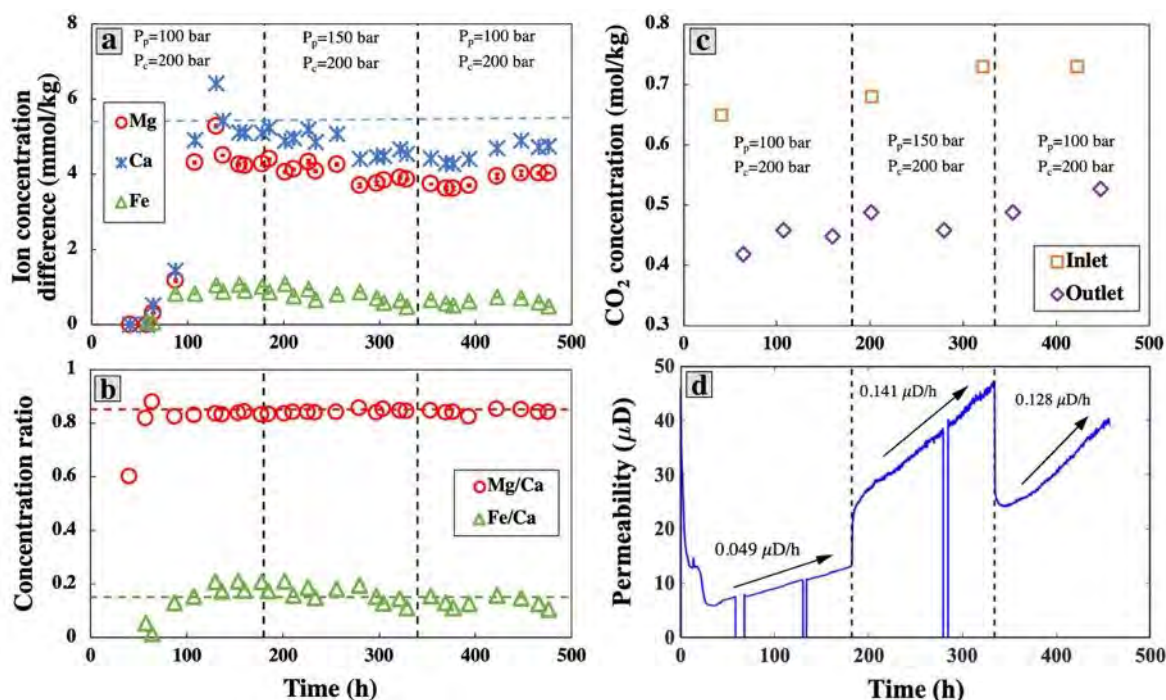


Figure 26: (a) Evolution of calcium (Ca), magnesium (Mg) and iron (Fe) molar concentration differences between the outlet and inlet fluids. (b) Evolution of the molar concentration ratios, Mg/Ca (red circles) and Fe/Ca (green triangles) during the reaction. (c) Evolution of CO₂ concentration in the inlet and outlet fluids. (d) Evolution of permeability during the reaction. P_p and P_c represent pore fluid pressure and confining pressure.

The progress of the fluid-rock reaction is illustrated in Figure 26(a), where the light blue dashed line indicates the maximum Ca concentration at the working conditions, under the assumption of equilibrium between CO₂-enriched brine (with a CO₂ concentration linearly increasing from 0.65 to 0.73 mol/kg as shown in Figure 26(c)) and dolomite, calculated using PFLOTRAN, indicating a near-equilibrium chemical state of the fluid. The molar concentration ratios Mg/Ca and Fe/Ca are stabilized at Mg/Ca=0.85 and Fe/Ca=0.15 (Figure 26(b)), suggesting stoichiometric dissolution of dolomite in the form of CaMg_{0.85}Fe_{0.15}(CO₃)₂. Except for the pressure build-up process in the first 40 hours, the measured bulk permeability keeps increasing during the reaction, as shown in Figure 26(d). The hourly increment rates of permeability ($\mu\text{D}/\text{h}$) at three different pressure conditions are also calculated and given on the plot (Fig. 26(d)). During this experiment, two dissolution passages formed in the sample, as shown in the X-CT images in Figure 27.

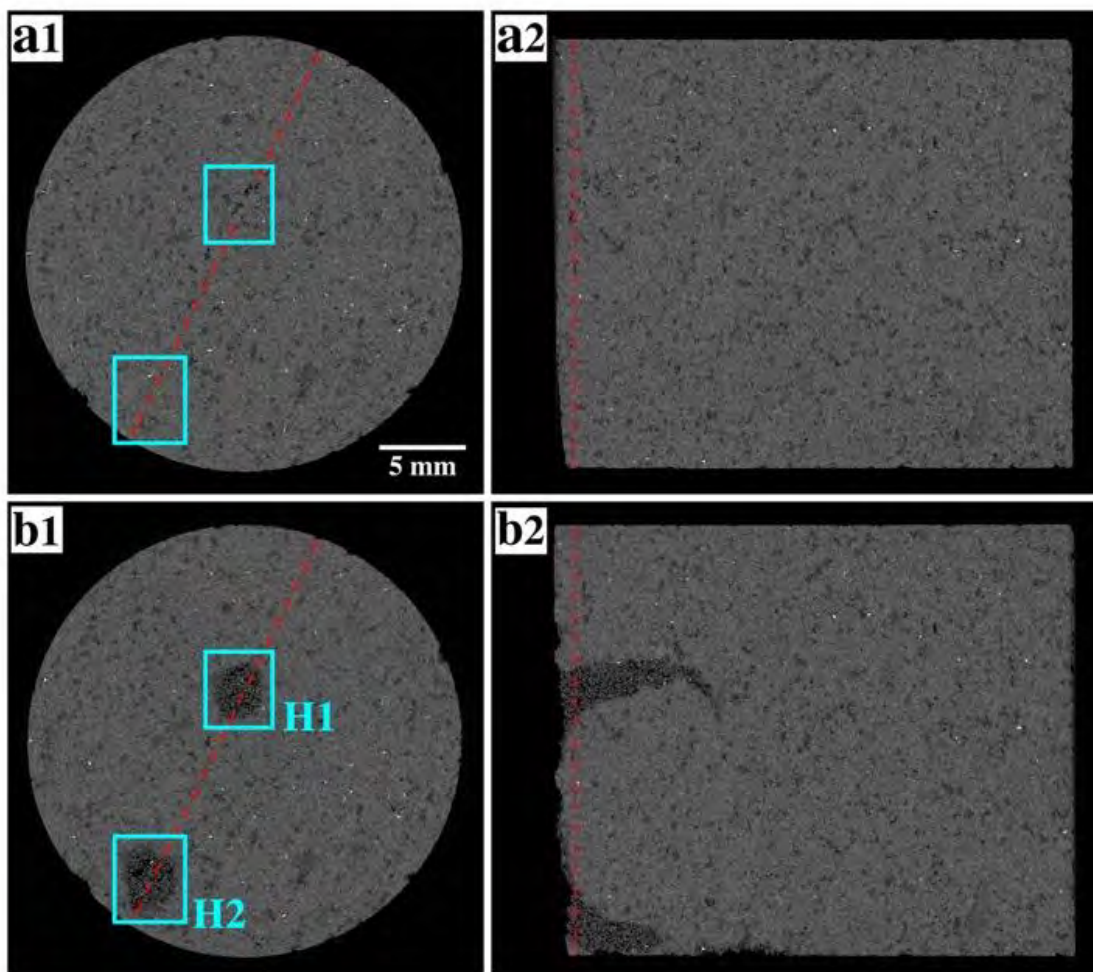


Figure 27: (a1) Pre-reaction X-CT cross section through the sample of sandstone from the Palanga-318a borehole, perpendicular to the flow direction. The position of this cross section is indicated by the red dashed line in (a2), at 1.2 mm from the inlet. (a2) Pre-reaction X-CT cross section through the same sample, parallel to the flow direction. The position of this cross section is indicated by the red dashed line in (a1). (b1) Post-reaction X-CT cross section through the same sample, perpendicular to the flow direction. The position of this cross section is the same as for (a1). (b2) Post-reaction X-CT cross section through the same sample, parallel to the flow direction. The position of this cross section is the same as (a2). The two porous passages, H1 and H2, created due to dolomite dissolution, are indicated by blue rectangles.

The bulk permeability, k , of this sample was measured under different confining pressures (P_c) and pore pressures (P_p) using 1 mol/l NaCl solution, before and after the reaction. As shown in Figure 28(a), a higher differential pressure, $\sigma_d = P_c - P_p$, leads to a lower bulk permeability. As a result of the

reaction (dolomite dissolution), the bulk permeability of the sample increased by 15-460% compared with the same pressure conditions before the reaction. Moreover, the effective stress for the permeability can be expressed as $\sigma_e = P_c - \alpha_k P_p$, where α_k is the effective stress coefficient, derived using the cross-plot method (Figure 29) introduced by Walsh in 1981. First, $\ln(k)$ is plotted as a function of P_p at a fixed P_c , as is shown as coloured solid symbols in Figure 29(a1) and (b1). Then, $\ln(k)$ is linearly regressed with respect to P_p . Within the measurement range of k , the P_p values at the intersections between the selected lines of equal $\ln(k)$ and the regressed lines are determined. For each iso-permeability line, the calculated P_p is then plotted against P_c in Figure 29(a2) and (b2), where the slopes represent the effective stress coefficient α_k . Using the calculated α_k , the relationship between permeability and σ_e is derived, as shown in Figure 28(b).

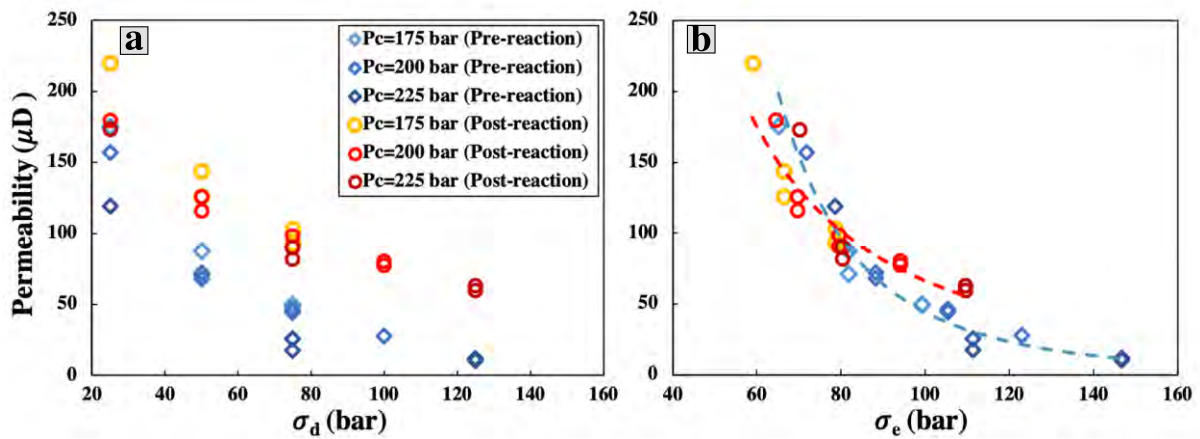


Figure 28: Permeability vs. σ_d and σ_e before and after the stimulation.

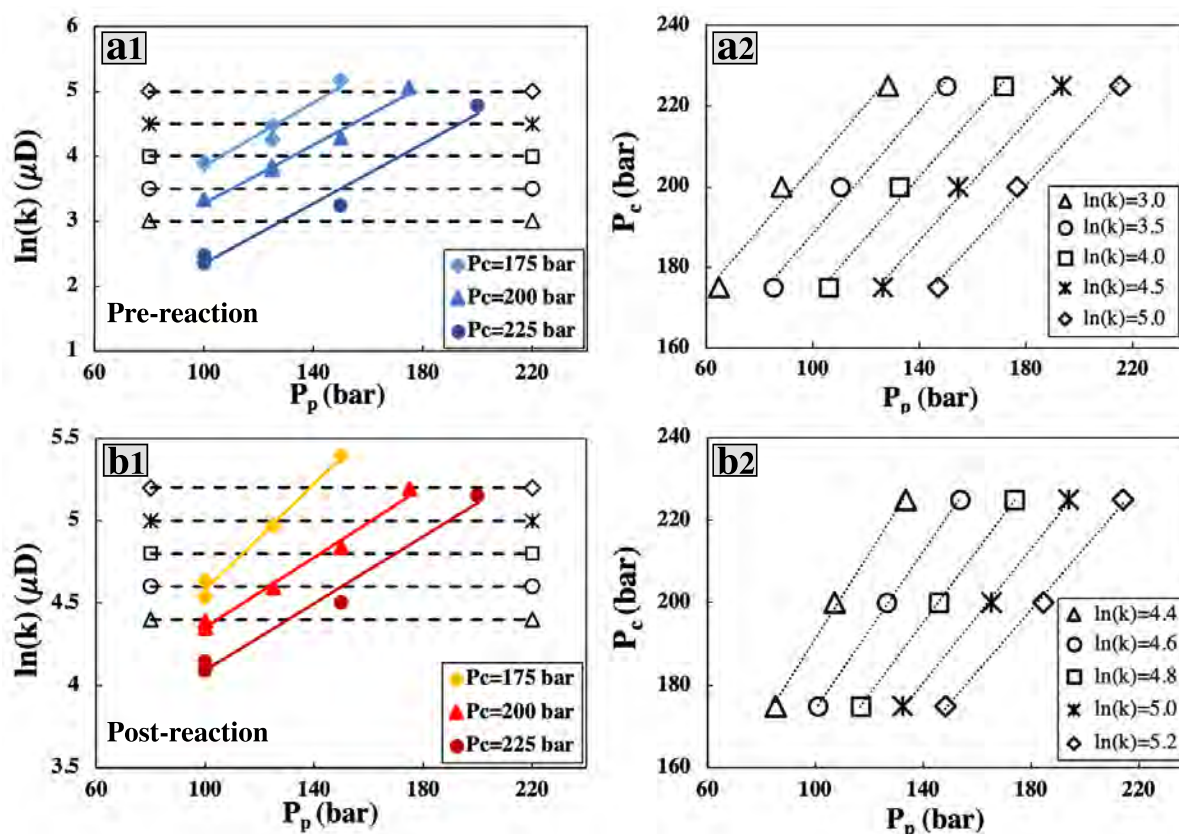


Figure 29: (a1) Pre-reaction permeability measurements plotted as $\ln(k)$ vs. P_p in colour (solid symbols), with linearly regressed solid lines. Dashed iso-permeability lines intercept the regressed solid lines, yielding the cross-plot in (b1). (a2) The same as (a1), but for post-reaction permeability measurements, yielding the cross-plot in (b2). (b1) The relationship between P_p and P_c along each iso-permeability line in (a1). The slopes of the dotted lines determine the pre-reaction effective stress coefficient α_k . (b2) The same as (b1), but for the post-reaction effective stress coefficient α_k .

1.3.7 Conclusions from flow-through experiments

Reactive flow-through experiments have been performed on two sandstone samples from the Vydmantai-1 and Palanga-318a boreholes. Chemical analysis of the Vydmantai sample provides a better understanding of the mechanism for dolomite cement dissolution, and suggests an effective reaction surface coefficient of 1% in this experiment. During the experiment using the Palanga sample, permeability changes caused by chemical reaction under different stresses were also studied. An increase in the effective stress coefficient was observed after the reaction, indicating a higher sensitivity of permeability to the pore pressure rather than to the confining pressure.

References

- Brehme, M., Nowak, K., Banks, D., Petrauskas, S., Valickas, R., Bauer, K., Burnside, N., Boyce, A. (2019). A review of the hydrochemistry of a deep sedimentary aquifer and its consequences for geothermal operation: Klaipeda, Lithuania. *Geofluids*, pp. 20. <https://doi.org/10.1155/2019/4363592>
- Brooks, R.A., Di Chiro, G. (1976). Beam hardening in x-ray reconstructive tomography. *Physics in Medicine & Biology*, 21, 390-398.
- Cnuddle, V., Boone, M.N. (2013). High-resolution X-ray computed tomography in geosciences: a review of the current technology and applications. *Earth-Science Reviews*, 123, 1-17.
- Ketcham, R.A., Carlson, W.D. (2001). Acquisition, optimization and interpretation of X-ray computed tomographic imagery: applications to the geosciences. *Computers & Geosciences*, 27, 381-400.
- Kiipli, E., Kiipli, T., Kallaste, T., Märss, T. (2016). Chemical weathering east and west of the emerging Caledonides in the Silurian – Early Devonian, with implications for climate. *Canadian Journal of Earth Sciences*, 53, 774-780.
- Noiriel, C. (2015). Resolving time-dependent evolution of pore-scale structure, permeability and reactivity using X-ray microtomography. *Reviews in Mineralogy and Geochemistry*, 80, 247-285.
- Pipira, D., Kostjukovs, J., Stinkulis, G. (2015). Mineral Composition and Morphology of Dolocretes of the Devonian Burtneiki and Amata Formations, Latvia. *Material Science and Applied Chemistry*, 32, 13-18
- Zinevicius, F., Sliupa, S., Mazintas, A., Dagilis, V. (2015). Geothermal Energy Use in Lithuania. 2015. Proceedings of the World Geothermal Congress, Melbourne, Australia 19-25 April 2015. Available at: <https://pangea.stanford.edu/ERE/db/WGC/papers/WGC/2015/01054.pdf>
- Zinevicius, F., Sliupa, S., Mazintas, A., Nika, N. (2020). Geothermal Energy Country Update - Lithuania. Proceedings of the World Geothermal Congress, Reykjavik, Iceland April 26 – May 2, 2020. <https://pangea.stanford.edu/ERE/db/WGC/papers/WGC/2020/01069.pdf>

2. Reservoir simulator development

Antoine Jacquey, Guido Blöcher

To optimize hydraulic-thermal-chemical (HTC) treatments proposed at DESTRESS demonstration sites, coupled simulation methods have been developed, capturing the relevant flow physics and chemistry from pore to reservoir scale. Detailed near-wellbore (e.g., pore-scale and meso-scale) and reservoir-scale modelling of HTC processes can be performed to demonstrate the enhancement of geothermal energy recovery at the stimulated sites (e.g. Klaipeda, Westland) through acidisation, or thermal shocks (cooling). The numerical models are populated with geological properties from detailed laboratory testing, as described in section 1 of this report. The overall goal of this combined laboratory-numerical approach is to determine relationships between chemical (and possibly thermal or even hydraulic) stimulation procedures and the resultant enhancement of fluid flow paths and permeability. Such insights may inform field scale procedures and feed into business models, designs and cost-benefit analyses of soft stimulations.

2.1 Thermal-hydraulic simulator for Klaipeda

A three-dimensional reservoir model has been developed for the Klaipeda site. This model incorporates geological information and physical properties for the relevant formations. Relevance of reactive transport has been identified by field and laboratory observations (DESTRESS Deliverable 6.1) but was not incorporated into the present modelling. The goals of the simulations were (1) to build a geological model which serves as backbone for future reactive transport models and (2) to constrain the temperature and pressure conditions within the reservoir and during operations, these being the main variables controlling the dynamics of reactive transport.

The reservoir model comprises three geological formations: a reservoir unit with an average thickness of 160 m, enclosed in between two clay and siltstone formations which serve as cap rock. The extent of this model is $\sim 6 \times 6 \times 0.2$ km. The geometry of the four wells at the Klaipeda site has also been integrated, based on available data. Figure 30 shows the geometry of this reservoir model and of the associated discretised finite element mesh.

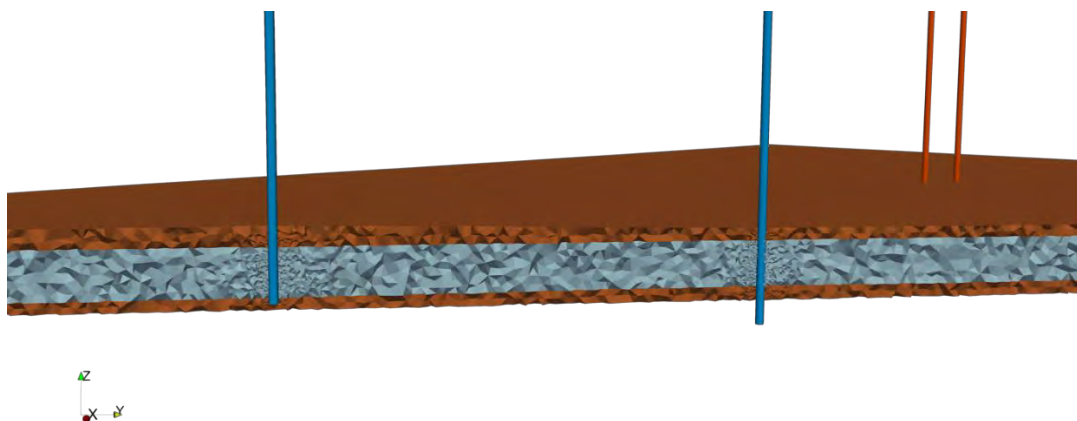


Figure 30: Reservoir model of the Klaipeda site and discretised finite element mesh with high refinement around the wells.

Steady state simulations have allowed values of parameters which were uncertain (for example thermal conductivity, or regional heat flow at the base of the reservoir) to be constrained, based on measurements in the wells. Figure 31 shows observations and numerical results for temperature and pore pressure in well Klaipeda-11. The good agreement indicates that the natural pressure/temperature conditions within the reservoir are well described by the model.

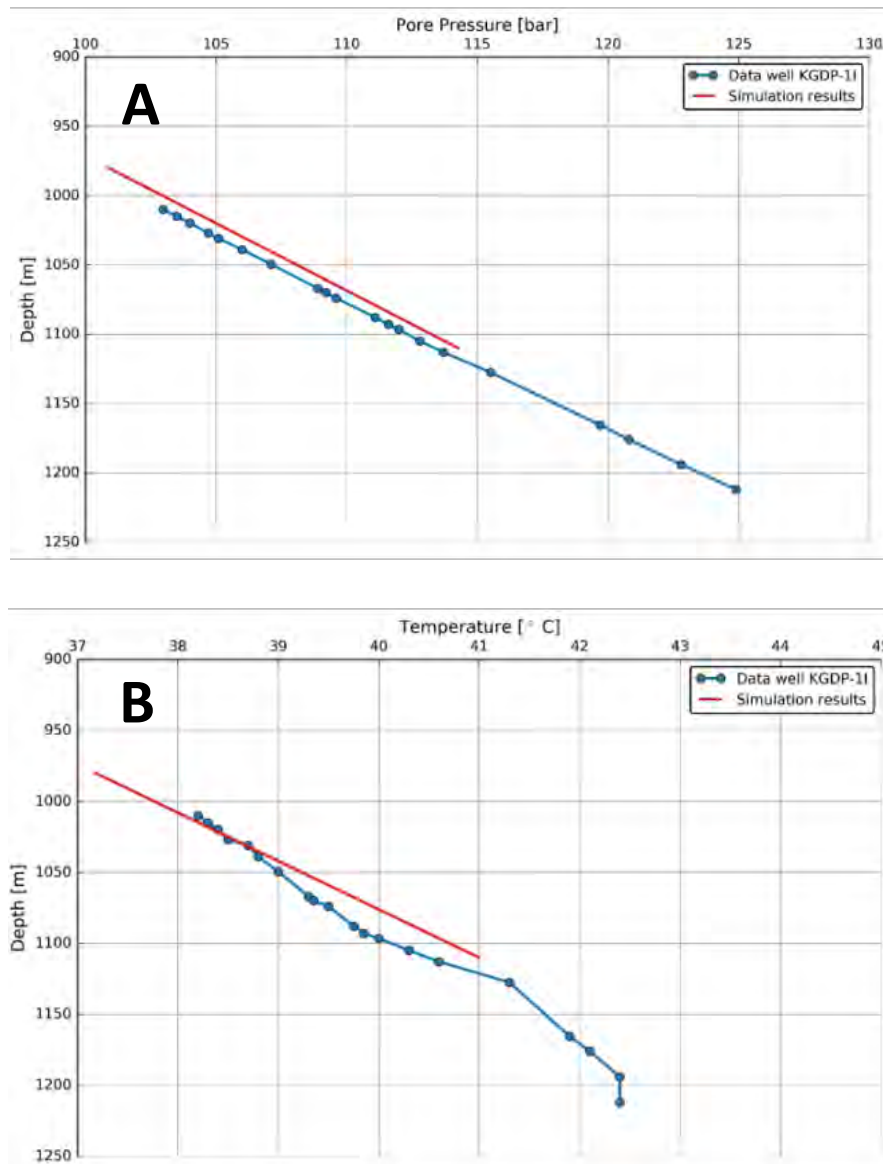


Figure 31: Comparison between observed and modelled pore pressure (A) and temperature distributions (B) in well KGDP-11.

Transient simulations have also been carried out using operational data (injection and production rates and injection temperatures) for the Klaipeda site between December 2000 and June 2006 (Figure 32).

Modelling of the Klaipeda site has improved understanding of the dynamic processes controlling temperature and pore pressure and provides a basis for future reactive transport modelling studies. The robustness of the numerical simulator is demonstrated.

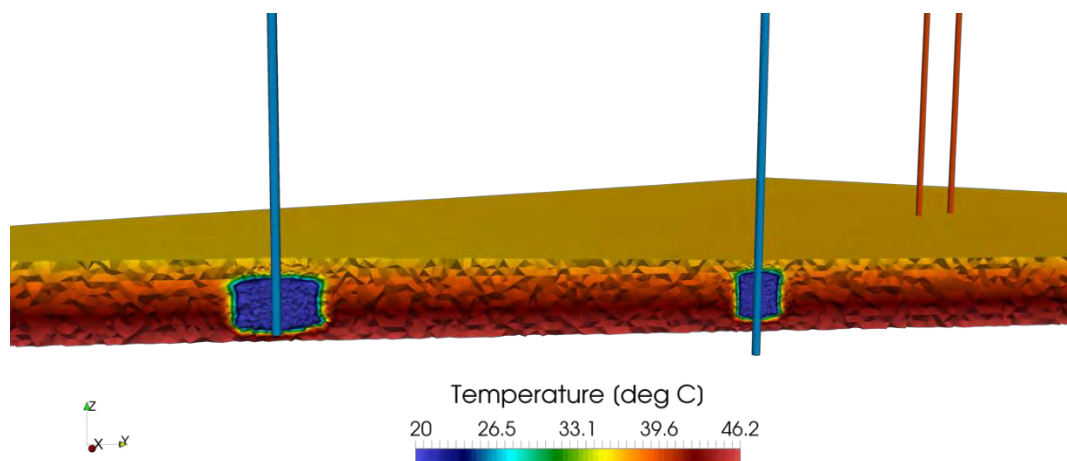


Figure 32: Distribution of temperature within the reservoir after two and a half years of modelled operations.

2.2 Thermal-hydraulic simulator for Mezőberény

Guido Blöcher and Cees Willems

A subsurface dataset from the Békés Basin in southeast Hungary formed the basis for the geological model for the Mezőberény site (Figure 1). As was discussed in subsection 1.1, this dataset consisted of two gamma-ray (GR) logs of the Mezőberény well doublet, three legacy GR logs of nearby petroleum wells, core fragments from five intervals of the Gyoma-1 well and six 2D seismic lines. Detailed facies realisations were generated using an object-based modelling approach in Schlumberger's Petrel 2018 software suite. To address the impact of sedimentary architecture on doublet performance, sandstone and shale facies were distributed in a shale matrix. The net sandstone-content in the model was constrained by facies interpretations of the well logs. Input parameters for this modelling include (1) net-to-gross volume proportions (i.e., proportions of sandstone and shale), (2) ranges of sandstone body width and thickness and (3) a range of palaeo-flow directions. It was assumed that the main palaeo-flow direction was from the northwest, with a 15° range. The top and base of the production interval formed the top and base of the aquifer model. The topography of these surfaces was constructed using dip trends from the seismic interpretations. A detailed description of the geological modelling and sedimentary architecture of the Pannonian Sandstones can be found in Willems et al. (2019). The dimensions of the resulting numerical model were 4500 m × 4500 m × 500 m. The injector-producer distance for the Mezőberény doublet is 1200 m. For numerical simulations of operation, injection/production rates were set at 10 m³/h for a duration of ~11 years. Reservoir property data were taken from the literature and from experimental work (section 1.1). As Figure 33 shows, the production simulations indicate that flow patterns are strongly influenced by porosity and permeability distribution and sedimentary aquifer architecture (see stream traces in Fig. 25). Flow follows sandstone beds within the reservoir, which are more permeable than the surrounding shale matrix. These initial simulations indicate that this model can be used to study doublet and well performance and for evaluation of increased porosity/permeability due to chemical stimulation.

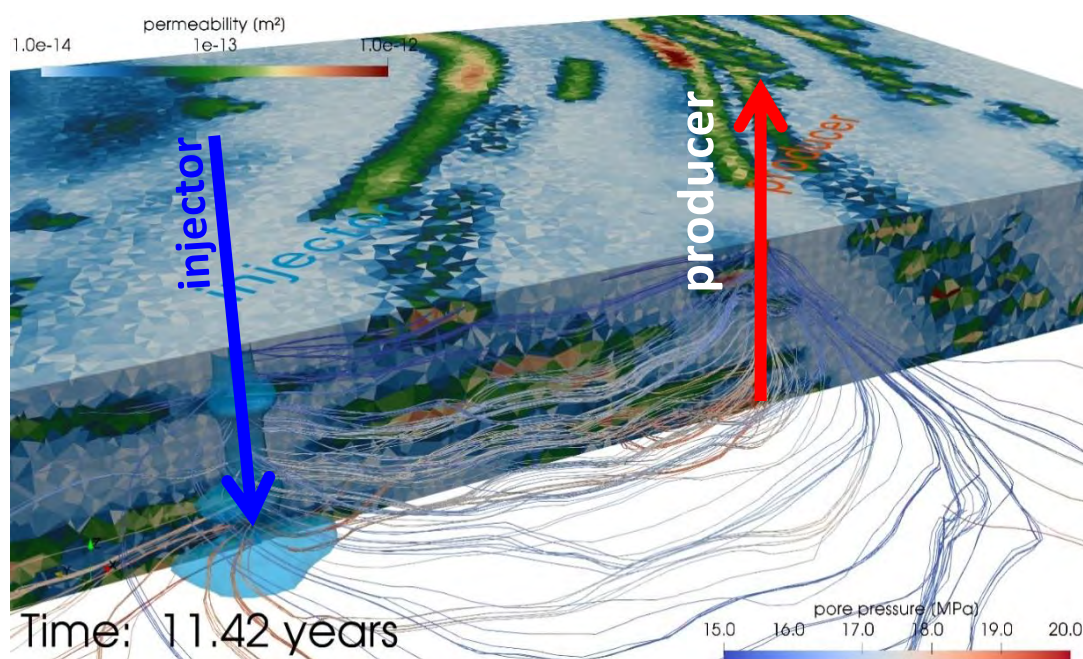


Figure 33: Stream traces and 30°C thermal front contour line around injector well after 11.4 years of simultaneous injection and production, considering a heterogeneous model reservoir in terms of porosity and permeability.

2.3 Thermal-hydraulic-mechanical simulator for Trias Westland

Nima Gholizadeh Doonechaly

A 3D thermo-hydro-mechanical model to investigate well and reservoir performance at Trias Westland has been built using COMSOL Multiphysics Solver, which provides numerical solutions for the equations for conservation of mass, momentum and energy in porous media (both rock matrix and faults). Mechanical effects are modelled assuming linear elasticity. Flow in both rock matrix and faults is formulated based on Darcy's law. The model consists of a rectangular block with side length 2.5 km representing the reservoir and confining layers above and below. The overlying layer is constrained by data whereas no clear/sharp boundary delineating the bottom layer is constrained by data (Figure 34). Reservoir layer thickness is set as 180 m and the thickness of the confining layers varies over the extent of the reservoir with a minimum of 100 m. The co-ordinates of the block corners are set so that the block orientation is consistent with the in-situ stress field extracted from offset well data. Faults are first converted to CAD surfaces and then discretely implemented in the model with zero thickness to improve computational efficiency. Therefore, the faults are considered as 2D objects in the model whereas fault thickness is considered in the mathematical formulation. The vertical extent of the faults is set equal to the extent of the confining layers above and below the reservoir layer. The fault thickness and permeability are set as 50 m and 50 mD. The stress boundary condition is initialized to the principal stress values extracted from available data as follows: vertical stress 90.23 MPa, minimum horizontal stress 57.2 MPa and maximum horizontal stress 72.8 MPa. The injection and production wells are also implemented in the model explicitly. A heat flux of 65 mW/m² is applied at the bottom of the model. A skin factor of -3 is also assumed for the injection well. To improve the computational efficiency, the balance equations are solved by direct solver using a segregated approach. The reservoir properties are set using data from publicly available sources from offset wells, from the literature, or assumed.

The first set of results showed that the thermal breakthrough has not yet occurred after 30 years of circulation of cold fluid through the model. These results also show that the predicted flow from the injection well to the production well is mainly via three faults, not through the reservoir rock matrix. The pressure impedance is predicted to increase rapidly during the first five years, then to increase at a slower rate.

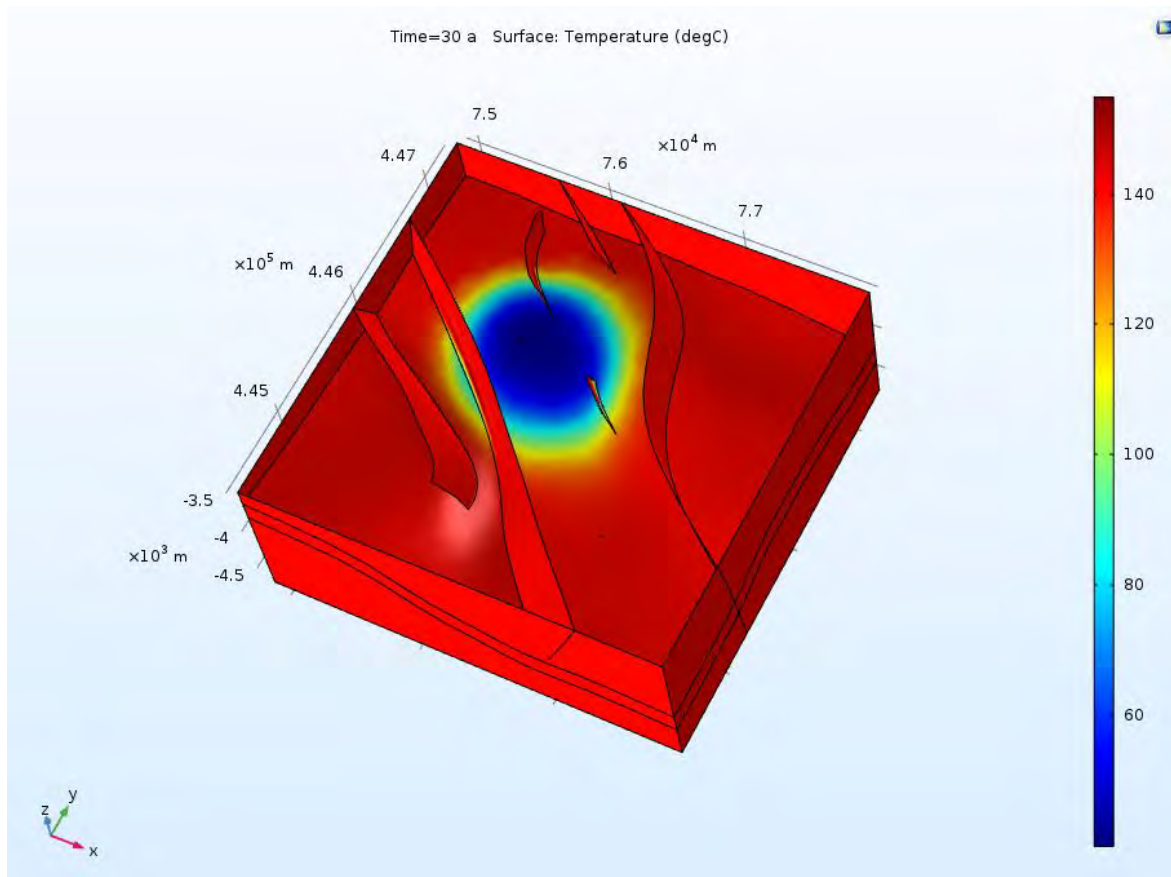


Figure 34: Modelled temperature distribution over the Trias Westland reservoir after 30 years of cold fluid circulation with an injection temperature of 40 °C.

2.4 Thermal-hydraulic simulator for Soultz-sous-Forêts

To simulate stress, pressure and velocity fields in the faulted granites at the Soultz-sous-Forêts site, a MOOSE (Multiphysics Object Oriented Simulation Environment) -based aquifer model in combination with GOLEM (Cacace and Jacquey, 2017) was developed. This allowed coupling of Thermal-Hydraulic-Mechanical processes. For the rock matrix, poroelastic behaviour was implemented (Cacace and Jacquey, 2017). For the fluid phase, the incompressible Navier-Stokes flow was implemented (Peterson, 2018). The Navier-Stokes module solves for the pressure and the velocity field inside the fault only. For the rock matrix, the primary variables are pore pressure and displacement. The fluid velocity in the porous matrix as well as the strain and stress field are derived from these primary quantities. To couple the fault system and the rock domain systems, four exchange functions along their interfaces were defined. Since fluid pressure inside the fault is solved almost instantaneously while the time scale of pore pressure diffusion in the rock is much longer, this pressure was used as the boundary condition for the pore pressure in the rock matrix (see (1) in Figure 35). Based on this pore pressure, the fluid velocity in the rock domain was calculated following Darcy's law. This fluid velocity was assigned as a slipping boundary for the fracture flow inside the fault (see (3) in Figure 35). To impose the mechanical coupling and the corresponding deformation of the fault, the displacement

values obtained in the rock matrix were assigned as boundary for the fault surface (see (4) in Figure 35). Since incompressible Navier-Stokes flow does not consider solid displacement as a primary variable, the displacement vector field was used to geometrically alter the fault mesh at each time step, resulting in a displaced mesh configuration that will update the final solution for the dynamic pressure and fluid velocity field. To derive a solution for the fault-rock system, the following initial boundary conditions were chosen. The initial condition for the rock matrix was zero pore pressure and displacement. The fluid pressure and velocity inside the fault were also set to zero. In addition to the boundary conditions applied at the interface, flow either in the x or y direction was imposed by setting the inlet pressure to 10 Pa. At the outlet, the pressure was held at zero throughout the simulation. At all other boundaries of the model fault and rock volume a no-flow boundary condition was imposed by setting the velocity vector to zero. For the mechanical part of the model, a zero displacement was assigned in the z -direction at the bottom of the model, also with zero displacement in the x - and y -directions for the lateral border, inlet and outlet. At the top of the model, i.e. along the z -direction, a compressive stress gradually increasing from 0 to 1 MPa was applied.

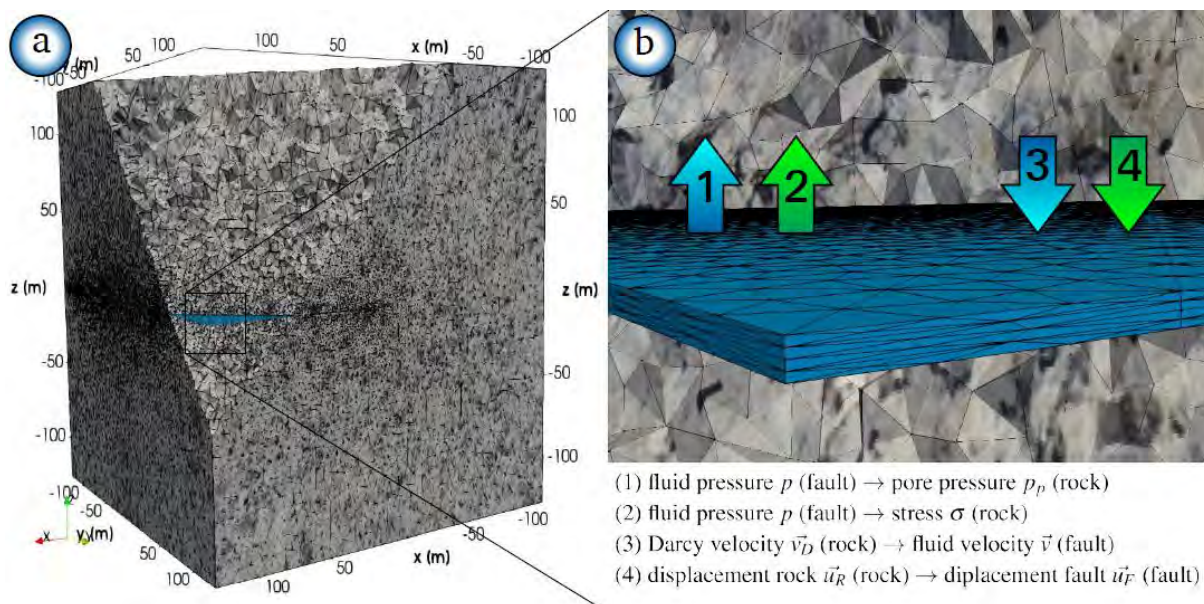


Figure 35: (a) Finite element generation of the fault and rock mass; (b) details of the transfer functions at the fault-rock interface.

The input structure of the model is a regular grid with a spacing of 1 m, dimensions of 512 m by 512 m, and a minimum aperture of 0 m. For the mesh generation a spacing of 4 m and dimensions of 256 m by 256 m were chosen. Considering a mean aperture of ~ 0.25 m, the fault aspect ratio is 1:1000. To mimic the precipitation of filling material in the fault (considered as coating), the two surfaces of the fault are interpenetrated stepwise from 0.059 m (case c0) to 0.199 m (case c7). This results in a contact area that varies between 14.3% and 65% for cases c0 and c7, respectively. Such an interpenetration causes sharp edges between the two surfaces, which will subsequently lead to many tetrahedral elements in the finite element mesh. To overcome this limitation, all fault apertures below 0.1 m were truncated. To represent the fault (aspect ratio 1:1000) in terms of a tractable number of tetrahedral elements (Figure 35a) we used an anisotropic mesh (Figure 35b). Normal to the fracture surface, the mesh was formed by a discretization of three-element layers at the fault tip and five-element layers at the wider part of the fault. Along the fracture, elements with an aspect ratio of 1:25 were introduced. Thus, the minimum element sizes were 0.033 m normal to the fault and 0.83 m parallel to the fault. For the rock volume an isotropic mesh was used with an element size of 0.83 m near the fault, coarsening with increasing distance. Tetrahedralization was performed using Gmsh (Geuzaine and

Remacle, 2009), a 3-D finite element mesh generator. The number of elements varies for the individual cases. For the fault, the number of tetrahedral elements ranged between 185,000 for case c7 and 730,000 for case c0. For the rock, the number of tetrahedral elements ranged between 1,886,000 for case c0 and 2,213,000 for case c7.

To quantify the impact of chemical soft stimulation in EGS reservoirs on the hydro-mechanical properties of the fault-rock system, which includes fault filling material, numerical flow-through experiments were conducted on a granite sample containing a single, partially sealed fault. Eight different scenarios for aperture were considered.

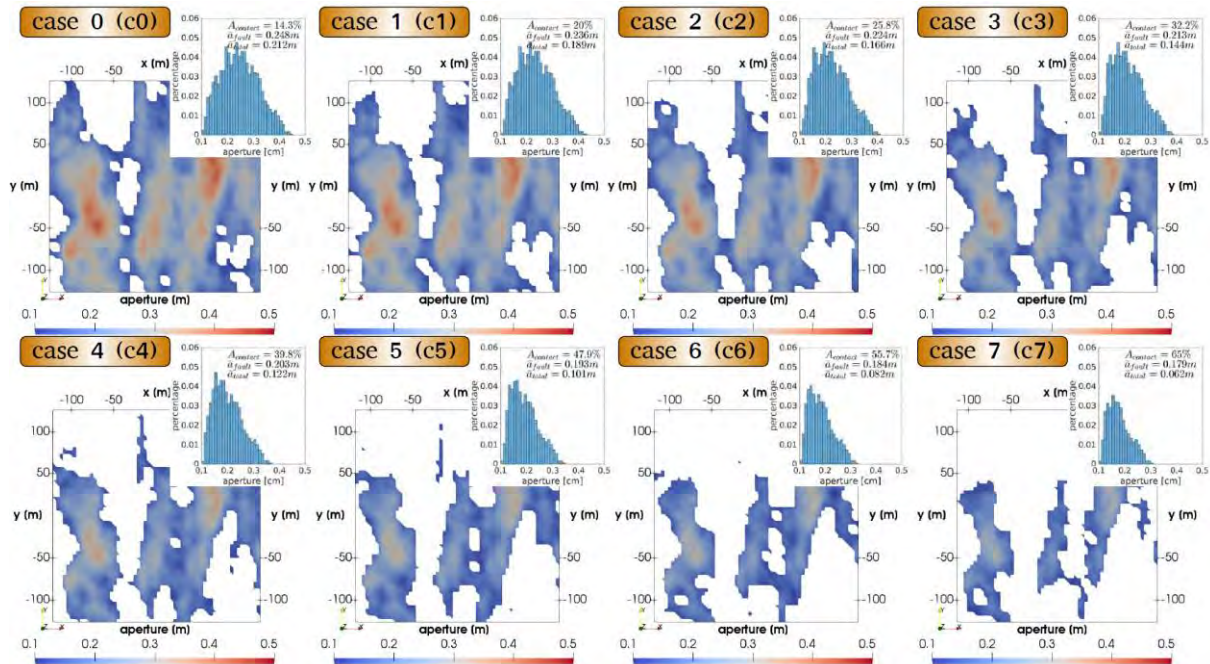


Figure 36: Aperture maps for simulation cases c0 to c7 during progressive steps of fault sealing, including the related histograms of aperture distribution.

Although a pressure gradient of only 10 Pa/256 m was applied, the volume flux through the fault was determined as 4.4 m³/s in the x-direction and 8.7 m³/s in the y-direction. The resulting permeability for case c0 was 2×10⁻⁶ m². This is the same order of magnitude that the relation between permeability (*k*) and aperture (*d*) relation $k = d^2/12$ would provide for millimetre scale aperture thickness. As a result of progressive sealing of the fault, the percolation threshold was reached, with the flow in the x-direction only, between cases c4 and c5 (Figure 37-h). This situation reduces the overall permeability to 2.15×10⁻¹⁶ m². In comparison, the rock permeability is 2.0×10⁻¹⁶ m². In contrast, the permeability in y-direction is only reduced from 3.4×10⁻⁶ m² (case c0) to 9.0×10⁻⁸ m² (case c7). The distribution of the velocity field in the fault-rock system indicates that the total permeability is dominated by the flow in the fault. Due to a strong channelling effect, a maximum flow rate of 0.5 m/s was observed at critical bottlenecks in the fault (Figure 37a,b,c,d). In contrast, the maximum flow rate in the rock matrix is ~10⁻¹³ m/s. Due to such low velocities in the rock matrix, it took almost 10 years for the model to reach a steady state pressure (Figure 37c,f) and velocity field in the rock domain. Assuming an applied stress of 1 MPa and the resulting total strain, the stiffness modulus of the fault-rock system is shown to be a linear function of the contact area along the fault zone. With increasing sealing of the fault, the stiffness modulus increases from 8 to 18 GPa (Figure 37). It can be approximated that the stiffness modulus will be close to the Young's modulus of the rock mass for a contact area of 100%. Besides the increase in the stiffness modulus, stress concentrations at the asperities of the fault were observed (Figure 37g). It is shown that these stress concentrations are in

the ratio of the applied stress at the top to the actual contact area along the fault. For case c3 (Figure 37g), with a contact area of 32.2%, the applied stress of 1 MPa gives a stress concentration of 5 MPa at the asperity boundaries (red domains).

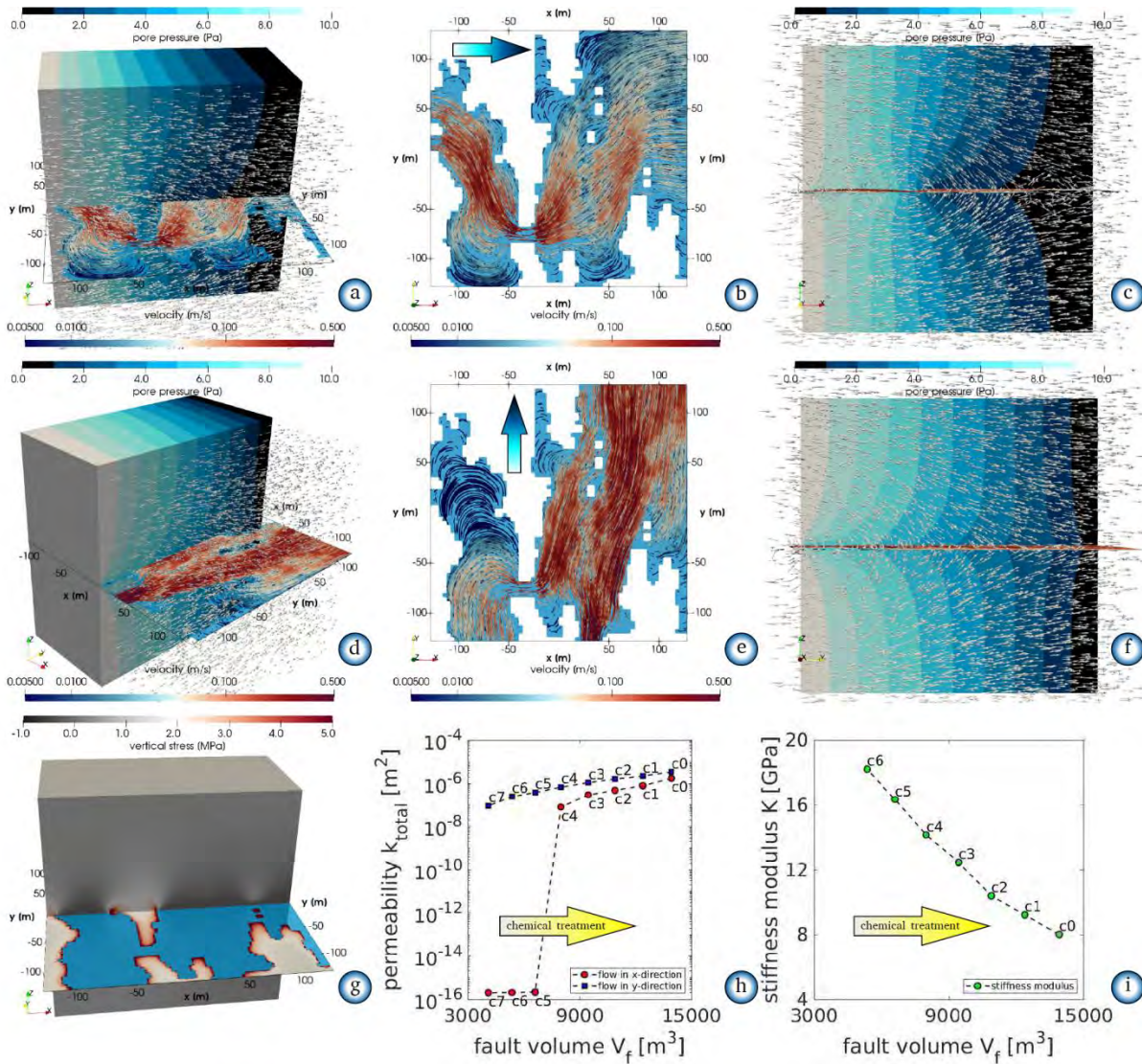


Figure 37 Simulation results: (a)-(c) pressure and velocity field for case c3 with imposed flow in x-direction; (d)-(f) in y-direction; (g) vertical stress distribution for case c3; (h) permeability evolution in the x and y directions as a function of the fault volume; (i) stiffness modulus of the overall system.

References

Cacace, M., Jacquey, A.B. (2017). Flexible parallel implicit modelling of coupled thermal-hydraulic-mechanical processes in fractured rocks. *Solid Earth*, 8, 921-941.

Candela, T. Renard, F, Klinger Y. Mair, K. Schmittbuhl, Brodsky, E.E. (2009). Roughness of fault surfaces over nice decades of length scales. *Journal of Geophysical Research, Solid Earth*, 117, B08409.

Geuzaine, C. Remacle, J.F. (2009). Gmsh: a 3-D finite element mesh generator with built in and pre- and post-processing facilities. *International Journal for Numerical Methods in Engineering*, 79, 1309-1331.

Peterson, J.W., Lindsay, A.D. Kong, F. (2018). Overview of the incompressible Navier-Stokes simulation capabilities in the MOOSE framework. *Advances in Engineering Software*, 119, 68-92.

Willems, C.J.L., Westaway, R., Burnside, N.M. (2019). Hydraulic Connectivity in Pannonian Sandstones of the Mezőberény geothermal doublet. *European Geothermal Congress 2019, The Hague, The Netherlands, 11-14 June 2019*.

3. Input data for the business plan - costs for stimulation

Cees Willems

Because actual stimulations did not take place at the Trias Westland and Mezőberény demonstration sites, this deliverable can only report cost estimates and analyses from Work Package 2 as input data for the business plan. Estimates of the cost of stimulation for the Trias Westland site were made by the site developer, Veegeo Energy, based on previous operations by this company and actual quotations that were acquired as part of the DESTRESS project. An overview of these costs is presented in Table 9.

Table 9: Estimated budget for the proposed Trias Westland stimulation

Service	Cost estimate	Amount	Costs	Remarks
<u>Stimulation services</u>				
Chemical + Pumping services	€ 270,000	1	€ 270,000	
Coiled tubing + Nitrogen Lift	€ 56,000	1	€ 56,000	
Neutralization acid	€ 20,000	1	€ 20,000	Estimation
<u>Acid Handling</u>				
Acid handling per m ³	€ 100	500	€ 50,000	Estimation based on previous quotations
Transport per m ³	€ 10	500	€ 5,000	Estimation based on previous quotations
<u>Overhead</u>				
Rig rate	€ 40,000	4	€ 160,000	1 day injection test 2 days stimulation 1 day injection test
Engineering + Project management per day	€ 1,000	20	€ 20,000	Estimation of needed hours for preparation
Contingency	€ 84,000	1	€ 84,000	15% of the total costs
		Total:	€ 665,000	

For the Mezőberény site, cost estimates only include costs of assessment of the state of the wells and logging to enhance geological data availability for further design of the actual stimulation. These costs (Table 10) were provided by GFZ, based on quotations from service companies.

Table 10 Estimated budget for logging and sampling to determine injection problems and the state of the Mezőberény wells.

Well site preparation	€14,300
Well integrity logging + mobilization equipment and personnel	€111,711
Logging: Continuous temperature Multifinger Caliper GR/CCL/RBT Radial Cement Bond Log G-G Gravel GR/Dual space neutron	€36,230
Fluid Well sampling	€31,890
Waste management	€28,007
Crane operation (7 days, incl. 2 days mobilization)	€9,060
Coordination and technical lead (5 days)	€10,596
Wellhead	€24,190
Wellhead assembling	€3,531
TOTAL	€269,516

Stimulation costs for the treatment at Soultz-sous-Forêts were not available at the time of writing of this report. These costs will be reported for DESTRESS Milestone 5.

4. Conclusions

This report presents preparatory work for the design and business planning for soft stimulation of poorly performing geothermal wells. It covers experimental and analytical approaches that have been used to determine site specific injectivity challenges and provide detailed geological properties for base-line monitoring of geothermal well performance. Experimental work has provided the following insights for the three demonstration sites covered by the present reporting.

4.1 Experimental rock characterization Mezőberény:

- Thin section analyses of fine-grained sandstones and siltstones in the Hungarian Újfalu Formation can contain abundant calcite cement that significantly reduces porosity. This facies will have a similar Gamma Ray log signal to higher porosity sandstone intervals but have almost no permeability and therefore result in a significant risk of overestimating suitability of rock properties. This could explain the unexpectedly poor performance of intervals that appear sandstone-rich.
- SEM analyses indicate presence of kaolinite clay in core samples of the Pannonian Sandstones. These introduce a potential injectivity risk as they are easily mobilised when the salinity of the injection water is not appropriate. After mobilisation they could clog pore space elsewhere in the aquifer and reduce the performance of the well doublet.
- Permeability did not significantly increase in the reactive flow-through experiments on sample H4, while calcite dissolution due to the acid treatment injection was apparent. Most likely this is because of the migration of fines that clog up pore space after they have been mobilised.

Table 11: Outcomes of experimental work related to the Mezőberény demonstration site. See Table 1 for explanation of the abbreviations. H5 outcomes are left out because only thin section analyses were carried out for this sample. (*) denote measurements that are ongoing at the time of reporting.

sample	H1	H2	H3	H4	
Well	Gyoma-1	Gyoma-1	Gyoma-1	Kond-1	
Depth [m]	1990-1995	1990-1995	1910-1913	1500	
Facies	siltstone	siltstone	Medium grained sst.	Fine-grained sst.	
Analyses					Property
X-CT			18% std:0.6% min-max: 17-20%		Porosity
MIP	*		*	*	Porosity + density
DSC	*		*	*	Heat capacity
LTA	*		*	*	Thermal conductivity
Reactive flow-through				<1 mD	Permeability
Numerical flow-through simulation			$k(\text{mD}) = 2e6 \cdot \phi^3 - 823465\phi^2 + 145094\phi - 8604.6$		Permeability-porosity relation
GP			38%	9.71%	Porosity

4.2 Experimental rock characterization Klaipeda:

X-CT analysis has provided an indication of the porosity of outcrop samples and borehole cores of Devonian sandstones in the study area. Results show that while both sets of samples are similar in mineralogical composition, the porosity is higher at outcrop than at reservoir conditions in the Klaipeda-1I and Vydmantai-1 wells. However, the samples obtained from the Palanga-318a well show a greater similarity to those at outcrop and indicate less influence of cementation or clogging of pores with pervasive clay minerals. The two samples from the Vydmantai-1 well are well cemented with initial estimates of porosity of 3.11% and 9.60%. These results suggest that burial depth could have influenced cementation and porosity. Because of the limited resolution of X-CT scanning, confirmation of the porosity measurements using experimental methods such as Mercury Intrusion Porosimetry or Gas pycnometry is required to confirm porosity calculations.

Mineral composition and porosity have been determined for the Vydmantai and Palanga sandstone samples. In addition, reactive flow-through experiments have been performed using these samples. A chemical analysis of the Vydmantai sandstone sample provides a better understanding of the mechanism of dolomite cement dissolution and suggests an effective reaction surface coefficient of 1% in this flow-through experiment. During the flow-through experiment using the Palanga sample, permeability changes caused by chemical reaction under different stresses were also studied. An increase in the effective stress coefficient was observed as a result of the reaction, indicating a higher sensitivity of permeability to the pore pressure than to the confining pressure.

4.3 Experimental rock characterization Westland:

The hydro-mechanical properties of the Triassic sandstone targeted by the Trias Westland project indicate that this reservoir is too tight to be considered for geothermal energy. Flow rates will be negligible unless the low reservoir permeability is restricted to the near well area or high permeability zones exist that can be connected to wells using stimulation treatments. Core samples from this reservoir provided an excellent opportunity to study the effect of stimulation, including the effect of subcritical crack growth on permeability and strength. Further results on these triaxial experiments are reported in DESTRESS deliverable 4.2.

4.4 Simulator development

Tailor-made reservoir simulators have been developed for the demonstration sites at Mezőberény, Klaipeda, Soultz-sous-Forêts and Westland. These allow long term forecasting of hydraulic-thermal-chemical (HTC) treatment to provide input data for soft-stimulation business plans. Coupled simulation methods were developed, capturing the relevant flow physics and chemistry at different scales, from pore to reservoir scale including the near-wellbore scale.

Mezőberény: Flow patterns are strongly influenced by the sedimentary aquifer architecture. Injection/production occurs in sandstone compartments of the aquifer that act as highly permeable layers in an impermeable shale matrix. Validation of this simulator will be possible with field data from the planned stimulation in the spring of 2020, and will be covered by later reporting.

Soultz-sous-Forêts: The impact of chemical soft stimulations on fault permeability in granite EGS reservoirs was evaluated by conducting numerical flow-through experiments. Chemical alteration of the fault aperture was approximated by sequentially changing the distribution pattern of fault-filling material using a hydro-poroelastic coupled simulation. Full details of the DESTRESS activities relating to chemical stimulation at Soultz-sous-Forêts will be reported for DESTRESS milestone 5.

Klaipeda: A three-dimensional reservoir model was developed for the Klaipeda site. Steady state simulations were conducted to replicate field production data. Good agreement between observations

and numerical results was established. Further application or validation of this simulator will not be conducted because demonstration of soft stimulation was postponed indefinitely, as financial difficulties led to withdrawal of the site operator from the DESTRESS project.

Westland: A 3D thermo-hydro-mechanical model was built to investigate the impact of stimulation using linear elasticity. Further application or validation of this simulator will not be conducted because demonstration of soft stimulation was cancelled, as the site operator decided not to pursue exploitation of the Triassic reservoir and withdrew from the DESTRESS project.

Imprint

Project Lead	GFZ German Research Centre for Geosciences Telegrafenberg 14473 Potsdam (Germany) www.gfz-potsdam.de/en/home/
Project Coordinator	Prof. Ernst Huenges huenges@gfz-potsdam.de +49 (0)331/288-1440
Project Manager	Dr. Justyna Ellis ellis@gfz-potsdam.de +49 (0)331/288-1526
Project Website	www.destress-h2020.ch
Copyright	Copyright © 2020, DESTRESS consortium, all rights reserved

Liability claim

The European Union and its Innovation and Networks Executive Agency (INEA) are not responsible for any use that may be made of the information any communication activity contains.

The content of this publication does not reflect the official opinion of the European Union. Responsibility for the information and views expressed in the therein lies entirely with the author(s).

DESTRESS is co-funded by

National Research Foundation of Korea (NRF)
Korea Institute for Advancement of Technology (KIAT)
Swiss State Secretariat for Education, Research and Innovation (SERI)